# NOAA
# NESDIS

NOAA TECHNICAL REPORT NESDIS 163

https://doi.org/10.25923/r4zh-xs14

# Report for Dedicated JPSS VIIRS Ocean Color Calibration/Validation Cruise: U.S. West Coastal Ocean in March 2023

Michael Ondrusek, Jianwei Wei, Menghua Wang, Eric Stengel, Charles Kovach, Alex Gilerson, Joaquim I. Goes, Chuanmin Hu, Sherwin Ladner, Nick Tufillaro, Kenneth J. Voss, Alexander Bailess, Andrew Barnard, Riley Blocker, Samuel Bunson, Jennifer Cannizzaro, David English, Helga do Rosario Gomes, Eder Herrera, Jamon Jordan, Maria Kavanaugh, Mateusz Malinowski, Wave Moretto, and Sarah Sullivan

**US DEPARTMENT OF COMMERCE**
**National Oceanic and Atmospheric Administration**
**National Environmental Satellite, Data, and Information Service**
**Center for Satellite Applications and Research**
**College Park, MD**
**April 2025**

# Report for Dedicated JPSS VIIRS Ocean Color Calibration/Validation Cruise: U.S. West Coastal Ocean in March 2023


Michael Ondrusek[1] (https://orcid.org/0000-0002-5311-9094)
Jianwei Wei[1,2] (https://orcid.org/0000-0002-6872-3534)
Menghua Wang[1] (https://orcid.org/0000-0001-7019-3125)
Eric Stengel[1]
Charles Kovach[1,2] (https://orcid.org/0000-0001-9249-2863)
Alex Gilerson[3]
Joaquim I. Goes[4] (https://orcid.org/0000-0002-9785-6985)
Chuanmin Hu[5] (https://orcid.org/0000-0003-3949-6560)
Sherwin Ladner[6]
Nick Tufillaro[7] (https://orcid.org/0009-0006-2896-8832)
Kenneth J. Voss[8] (https://orcid.org/0000-0002-7860-5080)
Alexander Bailess[7]
Andrew Barnard[7] (https://orcid.org/0000-0002-3664-3193)
Riley Blocker[8] (https://orcid.org/0000-0003-3278-4527)
Samuel Bunson[5]
Jennifer Cannizzaro[5] (https://orcid.org/0000-0002-9536-6333)
David English[5] (https://orcid.org/0000-0003-1560-8513)
Helga do Rosario Gomes[4] (https://orcid.org/0000-0002-6287-354X)
Eder Herrera[3]
Jamon Jordan[7]
Maria Kavanaugh[7] (https://orcid.org/0000-0001-6126-6177)
Mateusz Malinowski[3]
Wave Moretto[7]
Sarah Sullivan[5]

[1] NOAA Center for Satellite Applications and Research, College Park, MD, USA
(https://www.star.nesdis.noaa.gov)

[2] Global Science & Technology, Inc., Greenbelt, MD, USA
(https://www.gst.com)

[3] City University of New York, New York City, NY, USA
(https://www.cuny.edu)

[4] Lamont Doherty Earth Observatory, Palisades, NY, USA
(https://lamont.columbia.edu)

[5] University of South Florida, St. Petersburg, FL, USA
(https://www.stpetersburg.usf.edu)

[6] Naval Research laboratory, Stennis Space Center, MS, USA
(https://www.nrl.navy.mil/Our-Work/Field-Sites/NRL-South)

[7] Oregon State University, Corvallis, OR, USA
(https://oregonstate.edu)

[8] University of Miami, Coral Gables, FL, USA
(https://www.miami.edu)

NOAA Technical Report NESDIS-163
April 2025

**U.S. Department of Commerce**
Howard Lutnick, Secretary

**National Oceanic and Atmospheric Administration**
Vice Admiral Nancy Hann, NOAA Administrator

**National Environmental Satellite, Data, and Information Service**
Stephen Volz, Assistant Administrator for NESDIS

**Recommended citation**

Michael O., J. Wei, M. Wang, E. Stengel, C. Kovach, A. Gilerson, J. I. Goes, C. Hu, S. Ladner, N. Tufillaro, K. J. Voss, A. Bailess, A. Barnard, R. Blocker, S. Bunson, J. Cannizzaro, D. English, H. do Rosario Gomes, E. Herrera, J. Jordan, M. Kavanaugh, M. Malinowski, W. Moretto, and S. Sullivan (2025). Report for Dedicated JPSS VIIRS Ocean Color Calibration/Validation Cruise: U.S. West Coastal Ocean in March 2023. U.S. Dept. of Commerce, NOAA Technical Memorandum NESDIS-163, 60 p. doi:10.25923/r4zh-xs14

**Copies of this report are available from**

https://repository.library.noaa.gov/

## Table of Contents

## List of Figures

## List of Tables

## Preface

The Ocean Color Science Team at the NOAA Center for Satellite Applications and Research (STAR) is dedicated to the "end-to-end" production of high-quality, fit-for-purpose, remotely sensed ocean color products that are required and expected by all NOAA line offices as well as by external users, including state-level and regional users. The team has coordinated the ocean color calibration and validation (Cal/Val) field campaign since 2014 with an annual dedicated cruise over open oceans and coastal regions. The overarching goal of the Cal/Val campaign is to collect in situ ocean radiometric and bio-optical data that can be utilized for the assessment of satellite data uncertainty and calibration of the satellite data to achieve high data quality from satellite-derived ocean color products. The Cal/Val field campaigns have been receiving support from the Joint Polar Satellite System (JPSS), the Office of Marine and Aviation Operations (OMAO), and the STAR management. To date, nine cruises have been conducted, which cover the U.S. east and south coastal waters and the Hawaiian waters. The in situ Cal/Val efforts are proven essential for maintaining the integrity of NOAA's satellite ocean color data products, which undergo calibration changes in orbit, and for extending the applicability of synoptic water quality data products.

The U.S. west coast cruise in 2023 marked the eighth field expedition. The specific objective was to take in situ ocean color measurements from ship-borne platforms in the west coastal waters of the United States. The matchup data, together with previous data collections, is used to validate the Visible Infrared Imaging Radiometer Suite (VIIRS) observations from the Suomi National Polar-orbiting Partnership (SNPP), NOAA-20, and NOAA-21 satellites, which are the primary sources for NOAA operational remotely sensed ocean color data products. In addition, in situ ocean property data can also be used for evaluation and validation of ocean color products derived from other satellites, including the Ocean and Land Colour Instruments (OLCI) onboard the Sentinel-3A and Sentinel-3B satellites, and the Second-Generation Global Imager (SGLI) on the Global Change Observation Mission-Climate (GCOM-C) satellite. Following prior successful practices, we invited external collaborators, who are experts in satellite ocean color remote sensing, to participate in the field campaign. During the cruise, the participants were able to take measurements of a range of ocean optical and bio-optical properties simultaneously with the NOAA team. In this report, we summarize the field campaign and the accomplishment of each participating team, with a focus on the data collected during the cruise. All in situ data will be assembled by the NOAA Ocean Color Science Team for an in-depth intercomparison and post-analysis.

Through the NOAA mission of science, service, and stewardship, we strive to provide ocean satellite data products that improve our understanding of the global ocean and inland water optical, biological, and biogeochemical properties, which support research and applications to benefit society.

Menghua Wang, PhD
Chief, Marine Ecosystems & Coastal Branch, NOAA/STAR/SOCD

Paul DiGiacomo, PhD
Chief, Satellite Oceanography & Climatology Division (SOCD), NOAA/STAR

(This page is intentionally left blank)

## Abstract

The eighth JPSS VIIRS ocean color Cal/Val field campaign was carried out in the west coastal waters of the United States in March 2023. Onboard the NOAA Ship *Bell M Shimada*, the field team visited 28 stations off Oregon and Washington. The field observations were focused on the quantities presently amendable from the NOAA VIIRS ocean color observations. They consist of various apparent optical properties (AOPs), such as water-leaving radiance spectra ($L_w(\lambda)$), inherent optical properties (IOPs), such as light absorption coefficient ($a(\lambda)$) and backscattering coefficient of particles ($b_{bp}(\lambda)$), and water biological and biogeochemical properties, such as chlorophyll-a (Chl-a) concentration. Other quantities, such as in-water polarized radiance distribution, above-water hyperspectral polarimetry, and phytoplankton cell counts, were also obtained to help understand the remote sensing problem and develop improved and novel satellite ocean color data products. This document reports the field efforts and achievements of participating teams, with preliminary results. Data synthesis is underway and in-depth analysis will be performed by the NOAA/STAR Ocean Color Science Team.

# 1. Background

One primary task of the NOAA/STAR Ocean Color Science Team is to streamline the NOAA satellite ocean color data processing and to provide reliable ocean color environmental data records (EDR) needed by the NOAA mission, which improve our understanding of ocean biology and ecology, including inland waters. There are three sets of VIIRS instruments currently flying in space. The first VIIRS instrument was launched in 2011 onboard the SNPP satellite and has since been operational (2011–present). The second VIIRS sensor flies onboard NOAA-20 (2017–present). The latest one has been in orbit since 2022 onboard the NOAA-21 satellite (2022–present). Each VIIRS sensor collects visible, near-infrared (NIR), and shortwave infrared (SWIR) data. The VIIRS ocean color data products are being adopted for oceanic and atmospheric modeling and environmental monitoring, including weather forecast and marine fish tracking.

Satellite sensors like VIIRS measure the total radiance at altitudes of ~600–800 km. Only a small amount of radiance originated from oceans, while a significant contribution is from the atmosphere and ocean surface. A small error in the radiance measured at the top-of-atmosphere (TOA) can become large uncertainties in subsequently derived normalized water-leaving radiance ($nL_w(\lambda)$). To minimize this problem, vicarious calibration is required for the satellite ocean color instruments [*Wang et al.*, 2016; *Werdell et al.*, 2007; *Zibordi et al.*, 2025; *Zibordi et al.*, 2015]. To generate accurate water-leaving radiance spectra, it is requisite to estimate the scattering and absorption properties of gases, water molecules, and aerosols in the atmosphere and to account for the water surface reflection through an atmospheric correction (AC) procedure [*Gordon and Wang*, 1994; *IOCCG*, 2010; *Wang*, 2007]. The uncertainty involved in this process will propagate to normalized water-leaving radiance ($nL_w(\lambda)$) or remote sensing reflectance ($R_{rs}(\lambda)$) and eventually to high-level ocean color products, such as chlorophyll-a (Chl-a) concentration, diffuse attenuation coefficient at 490 nm ($K_d$(490)), suspended particulate matter (SPM), optical water classes, quality assurance, diffuse attenuation coefficient at the domain of photosynthetically available radiation (PAR) ($K_d$(PAR)), and various inherent optical properties (IOPs) [*Shi and Wang*, 2019; *Son and Wang*, 2015; *Wang and Son*, 2016; *Wei et al.*, 2016; *Wei et al.*, 2021; *Wei et al.*, 2022]. It is essential to evaluate the uncertainty of the satellite ocean color data products in different environments to understand their applicability.

The JPSS program has funded the VIIRS ocean color Cal/Val campaigns since 2014 to collect field data concurrent with the VIIRS overpass, which can be used to calibrate the VIIRS sensors and validate the VIIRS ocean color data products around the U.S. waters. To date, the Ocean Color Science Team has coordinated nine cruises successfully in the Mid-Atlantic Bight, South Atlantic Bight, Gulf of America, Hawaii, U.S. west coastal region, and U.S. southeast coastal region. A summary of the field efforts from the first seven cruises (2014-2022) has been published as NOAA technical reports [*Ondrusek et al.*, 2015; 2016; *Ondrusek et al.*, 2017; *Ondrusek et al.*, 2019; *Ondrusek et al.*, 2021; *Ondrusek et al.*, 2022; *Ondrusek et al.*, 2024] and book chapters [*Nalli et al.*, 2022; *Perez et al.*, 2022; *Wei et al.*, 2023]. The NOAA OMAO allocated ship time (SH-23-02) for the 8$^{th}$ annual cruise with the NOAA Ship *Bell M. Shimada* (Hull number R227) in early 2023. The primary objective of the cruise was to collect high-quality in situ apparent optical properties (AOPs), IOPs, and water biological/biogeochemical data, for the use in calibration and validation of the VIIRS ocean color radiometry and all other $nL_w(\lambda)$- or $R_{rs}(\lambda)$-derived products in the U.S. coastal waters.

# 2. Field Campaign

## 2.1. Objectives

The primary objective of the SH-23-02 expedition was to provide initialization validation data for the newly added VIIRS-NOAA-21 satellite, which was launched in November 2022. This was the first validation cruise since the NOAA-21 launch and these observations were required to understand the performance of the new VIIRS sensor. This was conducted by observing and measuring AOPs and IOPs of water masses for three primary objectives: 1) VIIRS ocean color satellite validation, 2) Inter-calibration and inter-comparison of validation techniques and measurements, and 3) optical characterization of ocean variability (i.e. coastal, near-shore, eddies, fronts, filaments, blue water, etc.).

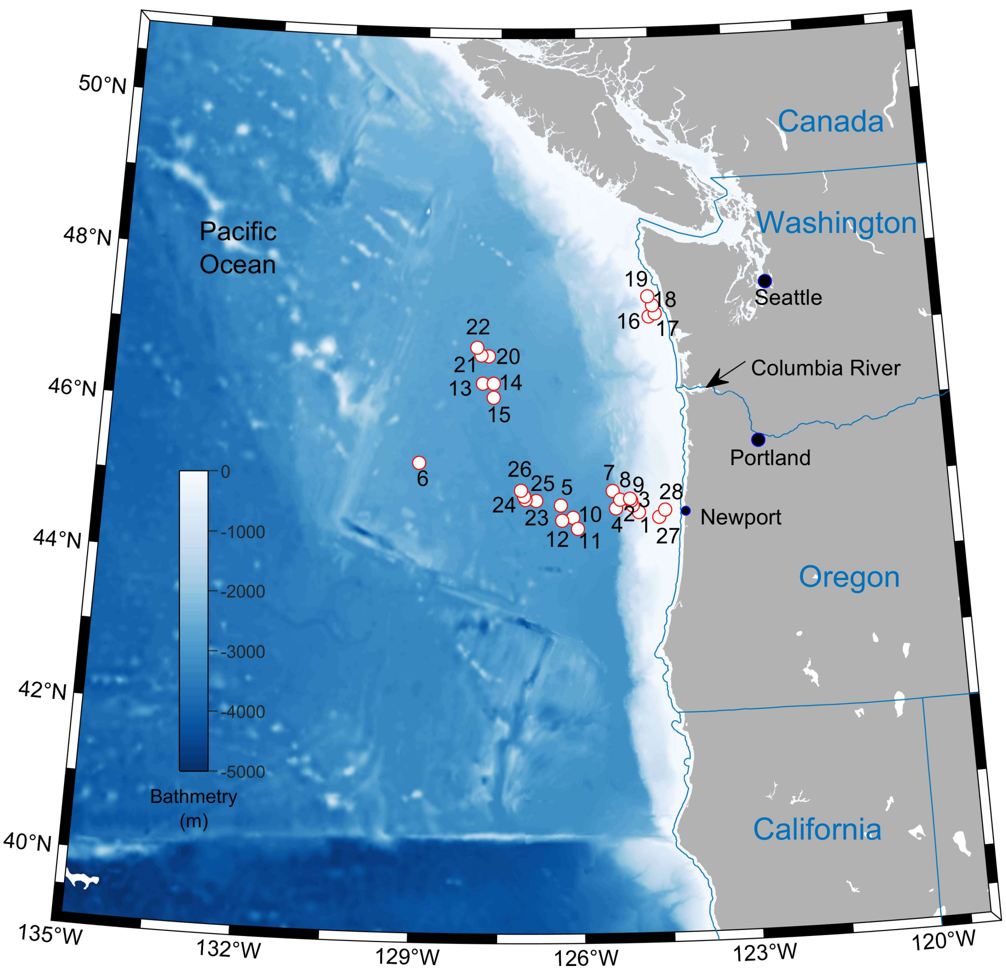


Figure 1. Study area of the VIIRS Cal/Val field campaign (SH-23-02) in March 2023. The sampling stations are indicated as closed circles, next to which the station numbers are given. The background image illustrates the bathymetric map in units of meters.

## 2.2. Study Area

The Cal/Val cruise was conducted within the northern California Current System (CCS), one of the biologically richest parts of the ocean [*Ryther*, 1969]. The field stations were confined between 44°N and 47.5°N and between the nearshore and up to ~350 km offshore of Washington and Oregon (Figure 1). The narrow continental shelf only extends a few tens of kilometers from the shore before transitioning to a steep drop-off to the deep ocean floor.

The northern CCS is featured with cool surface waters brought from the North Pacific Ocean and the Gulf of Alaska. The water temperature ranges from 13°C in winter to 18°C in late summer. Prevailing northwesterly alongshore winds induce upwelling, which lifts nutrient-rich deep water to the well-lit surface. The nutrients are consumed by phytoplankton and dramatically increase primary productivity in this region [*Hickey and Banas*, 2008]. The abundance of phytoplankton and zooplankton in turn attracts large populations of whales, seabirds, and important fisheries, creating a rich and diverse marine ecosystem.

According to the global water classification [*Wei et al.*, 2022], the water type is predominantly Class 4 in the offshore region and Class 8 in the nearshore region. Typically, Class 4 is characterized by low Chl-a values (around 0.3 mg $m^{-3}$) and low SPM values (around 0.25 mg $L^{-1}$). Class 8 is representative of more turbid waters, with higher Chl-a values (~0.9 mg $m^{-3}$) and higher SPM values (~0.45 mg $L^{-1}$). The field stations were designed to encompass both offshore clear waters and nearshore turbid environments.

## 2.3. Research Vessel

The NOAA Ship *Bell M. Shimada* is an American fisheries research ship in commission since 2010 (Figure 2). It operates along the U.S. West Coast and is homeported at the NOAA Marine Operations Center–Pacific in Newport, Oregon. It has a 55 $m^2$ wet laboratory, a 19 $m^2$ dry laboratory, a 25 $m^2$ chemistry laboratory, a 44 $m^2$ electronics and computer laboratory, and a 17 $m^2$ hydrographic laboratory. It has multiple scientific freezers, refrigerators, and store rooms. The ship has open deck space aft for scientific operations and open deck space on her starboard side. In addition to the ship crew of > 20, *Bell M. Shimada* can accommodate up to 15 scientists. *Bell M. Shimada* is capable of conducting multidisciplinary oceanographic operations in support of biological, chemical, and physical process studies. It is equipped with an Acoustic Doppler Current Profiler (ADCP) to collect data on ocean currents and a multibeam echo sounder system (MBES) that provides information on the content of the water column, the seafloor type, and topography. It has an oceanographic winch that can deploy up to 5100 meters, two hydrographic winches each of which can deploy 3600 meters, and two trawl winches deployable up to 4300 meters. The oceanographic CTD Rosette package is integrated with fluorometers, allowing for collecting water samples from multiple depths.


Figure 2. Picture of NOAA Ship *Bell M. Shimada* (Credit: Lt. Terril Efird, NOAA).


Figure 3. Cruise Participants. From left to right: Back row: Michael Ondrusek, Alex Bailess, Sherwin Ladner, Joaquim Goes, Eder Herrera, Matuesz Malinowski, Charles Kovach, and Riley Blocker. Front row: Samuel Bunson, Wave Moretto, Shefali Menezes, Sarah Sullivan, and Jamon Jordon. (Photo courtesy of Jamon Jordon).

## 2.4. Participating Institutions

- NOAA Center for Satellite Applications and Research (STAR), College Park, Maryland
- Naval Research Laboratory (NRL), Stennis Space Center, Mississippi
- City College of New York (CCNY), New York City, New York
- Oregon State University (OSU), Corvallis, Oregon
- Lamont-Doherty Earth Observatory (LDEO), Columbia University, Palisades, New York
- University of South Florida (USF), St. Petersburg, Florida
- University of Miami (Miami), Coral Gables, Florida

## 2.5. Personnel/Science Party

Table 1. List of science party personnel aboard NOAA Ship *Bell M. Shimada*.

| Name (Last, First) | Title | Affiliation |
|---|---|---|
| Ondrusek, Michael | Chief scientist | NOAA/NESDIS/STAR |
| Stengel, Eric | Marine Tech | NOAA/NESDIS/STAR |
| Kovach, Charles | Marine Tech | NOAA/NESDIS/STAR |
| Ladner, Sherwin | Researcher | NRL |
| Bailess, Alexander | Researcher | OSU |
| Jordon, Jamon | Researcher | OSU |
| Moretto, Wave | Researcher | OSU |
| Bunson, Samuel | Researcher | USF |
| Sullivan, Sarah | Researcher | USF |
| Goes, Joaquim | Researcher | LDEO |
| Herrera, Eder | Researcher | CCNY |
| Malinowski, Mateusz | Researcher | CCNY |
| Blocker, Riley | Student | Miami |
| Menezes, Shefali | Student | Seattle University |

## 2.6. Instruments and Calibration

### *2.6.1. Scientific instruments*

The scientific instruments are listed below, which are grouped by the deployment mode:

- Profiling optical radiometers
  - ✓ Hyperspectral free-fall optical profiler (HyperPro)
- Floating optical radiometers
  - ✓ Hyperspectral tethered spectral radiometer buoy (HTSRB)
  - ✓ Spectral polarized radiance distribution camera system (PixlPol)
- Above-water handheld radiometers
  - ✓ Analytical Spectral Devices, Inc. (ASD) radiometers
  - ✓ Spectra Vista Corporation (SVC) radiometers
  - ✓ Geophysical and Environmental Research Corp. (GER) radiometers
  - ✓ Spectral Evolution, Inc. (SEI) spectroradiometers
  - ✓ Snapshot hyperspectral imager
  - ✓ Polarization camera
- Profiling water sampling and optical packages
  - ✓ Conductivity, Temperature, and Depth (CTD) package
- Water samples/Rosette Collection/Lab Processing
  - ✓ Filtration Rigs
  - ✓ Benchtop fluorometer
- Flow-through instruments
  - ✓ Nine-band absorption and attenuation meter (AC-9)
  - ✓ Hyperspectral absorption and attenuation meter (AC-S)
  - ✓ Backscattering meter at three bands (BB-3)
  - ✓ Fluorescence Induction and Relaxation (FIRe)
  - ✓ Flow imaging microscope (FlowCam)
  - ✓ Custom Laser Spectrofluorometer (CLS)
- Atmospheric radiometers
  - ✓ Photosynthetically Available Radiation (PAR) sensor
  - ✓ Microtops II Ozone Monitor Sunphotometer
  - ✓ Global positioning system (GPS)

### *2.6.2. Calibration*

Pre-cruise calibrations were conducted in the NOAA College Park Calibration Lab on February 9, 2023, on the NOAA HyperPro and HTSRB sensors and the USF HyperPro Sensors. Post-cruise calibrations were conducted on the same sensors. No significant differences were observed between the pre- and post-cruise calibrations. Radiance sensors were calibrated with a National Institute of Standards and Technology (NIST)-traceable Optronic Laboratories OL-455 integrating sphere. Irradiance sensors were calibrated with a NIST-traceable FEL type 1000 W standard irradiance lamp.

### 2.7. Operation and Execution Plan

As the primary goal of these cruises is to validate VIIRS ocean color product data, the daily plan is centered on sampling radiometry within a few hours or as close as possible to VIIRS overpasses, which occur primarily at local times between 12:00 and 14:00. Each station requires approximately two hours to complete the measurement and a 10 NM distance is desired between stations on any particular day. Therefore, there is a time limitation to only allow for conducting 3 main stations per day. The first station is from 0900 to 1100 hr., there is approximately one hour of steaming to the next station, the second station takes place from 1200 to 1400 hr., and the third station is from 1500 to 1700 hr. Occasionally, there is time for a quick 4$^{th}$ station in the evening. Each station includes the above-water and in-water hyperspectral remote sensing reflectance measurements, the measurement of IOPs, and the collection of seawater for the measurement of derived ocean color products. The timing of the hyperspectral measurements of $R_{rs}$ are attempted to be made closest to the satellite overpass time. The in-water $R_{rs}$ measurements were HyperPro profilers and the floater was a HyperPro outfitted as a HTSRB. The above-water measurements were done using hand-held radiometers off the bow and were conducted mostly during the profile measurements. The on-station water collection was done by Niskin Bottles on the ship's Rossette. This cast and the IOPs cast were operated off the J-frame and these measurements are essentially independent of the current light field. Therefore, the morning station sampling order is J-frame (Rosette and IOPs), then floaters, then profilers to provide $R_{rs}$ measurements closest to the satellite overpass. The sampling order for the mid-day and 3$^{rd}$ stations is profilers, floaters, and then J-frame.

This was a challenging project out of the first eight VIIRS Cal/Val cruises with snow on shore and high winds offshore. In addition, clouds dominated the entire study area during the cruise. Even when there were narrow band openings or small holes in clouds, these cloud features were always spotty and moving rapidly, making predictions difficult and collecting matchups challenging (Figure 4, Figure 5, and Figure 6). The primary tool for predicting clear sky locations was https://www.windy.com. This application gives full ocean predictions of wind, clouds, and sea state up to 10 days in advance. Five different model predictions are given and are updated every few hours. Therefore, prediction accuracy increases the closer in time to the sampling day. In a broader overview, our cruise track has to be guided by the final destination. When departing from one port and ending in another, there was less ability to deviate from the planned cruise track to encounter predicted clear skies as there is a timeline to be at the destination. This pathway has more flexibility when the port of departure and the arrival port are the same, but a timeline still has to be followed. In these situations, the ship can transect a certain distance from the port only limited in distance by the time it takes to return. Sampling on the station only occurs between 0900 and 1700 hr. This leaves approximately 16 hours to steam at 8 to 10 kn overnight to a new location. Typically, along with required ship operations, approximately 130 NM can be covered overnight to find clear sky locations that are aligned with the cruise plan.

### 2.8. Daily Activities

The Cal/Val Cruise took place out of Newport, Oregon from March 2 to 11, 2023. The original plan was for 14 days at sea (DAS) scheduled for February 26 to March 11, 2023, with staging for the cruise to start on February 24. However, there was a 100-year snowstorm on the west coast starting on February 23, 2023, the day the team was flying to Oregon. Portland airport and most of the west coast airports were closed and team members were held overnight in Denver and other locations. On the next day, the NOAA team had to change plans to fly to Eugene, OR instead of Portland. It was the only way to get there by March 3 and the luggage did not make it. Most team members had similar delays including getting liquid nitrogen and a foreign national clearance. The ship was scheduled to leave on Sunday, February 26, 2023. However, that afternoon they were expecting 20 kn winds going up to 30 kn with rain and 15 ft seas. These conditions were expected to last through Tuesday, February 28, and the first day the ship could depart was Wednesday, March 1. Due to ship mechanical delays, we could not get out until Wednesday evening.

- The first sampling day was March 2$^{nd}$. Three stations were occupied directly offshore from Newport in green waters and encountered suboptimal conditions with 10 ft seas, 15 kn winds, and > 50% cloud cover. Clear sun locations for the three stations were found and good matchups with SNPP, NOAA-20, and NOAA-21 for Stations 1 and 3 were observed.

- On March 3$^{rd}$, the ship steamed about 40 NM offshore trying to find a predicted hole in clouds but encountered 17 ft. seas, complete cloud cover, and >20 kn winds. Only one station (Sta. 4) was occupied with no satellite matchups.

- On March 4$^{th}$, *Bell M. Shimada* headed 200 NM offshore in an attempt to get clear-sky conditions but encountered 18 ft seas, 20 to 25 kn winds, and spotty 50% cloud cover. Stations 5, 6, and 6B were occupied. Only a few occupied pixels at stations 6 and 6B were observed by the satellites.

- On March 5$^{th}$, the ship headed back toward Newport near the stations from the first day for stations 7, 8, and 9. Despite fast-moving spotty clouds covering ~50% of the sky, some satellite matchups were obtained for all three stations. Overnight on the 5$^{th}$, the ship headed offshore again in search of the elusive clear-sky conditions at a location 80 NM from Newport to a spot predicted to potentially have a small clear sky during overpass times.

- During the day on March 6$^{th}$, stations 10, 11, and 12 were occupied at one of the best locations in the area but still encountered fast-moving clouds, 7 to 10 ft. seas, and 10 kn winds. Matchups were obtained for all three VIIRS sensors though all had straylight flags due to the proximity to nearby clouds (Figure 4).

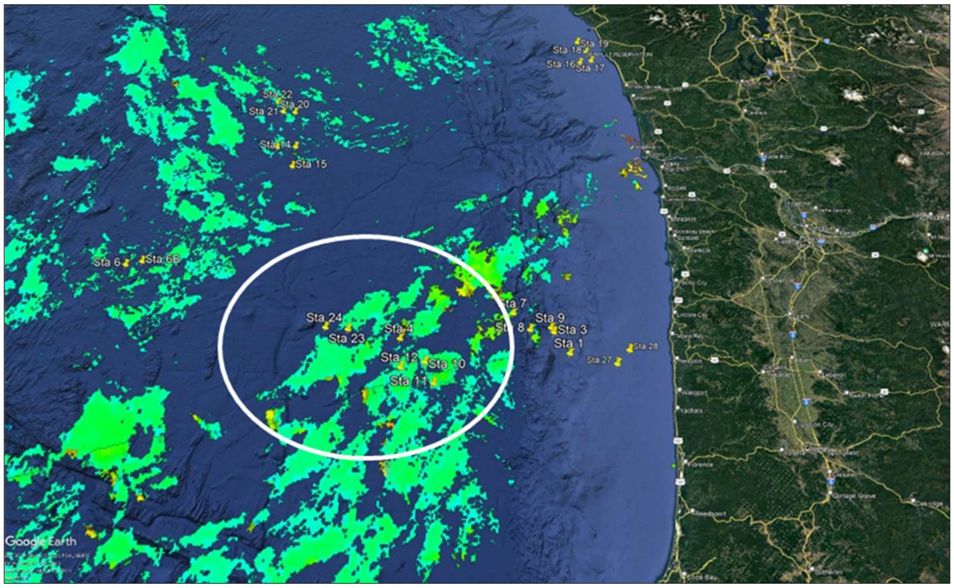

Figure 4. Satellite Chl-a image (March 6, 2023) showing stations 10, 11, and 12.

- *Bell M. Shimada* traveled 100 NM north overnight for a predicted clear-sky hole in clouds on March 7th for stations 13, 14, and 15. However, a large cloud covered the entire sampling area, and no matchups were obtained.

- On March 8th, the ship headed 130 NM northeast to productive waters just off the coast near Seattle (Figure 5). This coastal area was the only location predicted to be cloud-free. Stations 16, 17, 18, and 19 were sampled in favorable conditions with 2 ft seas, 10 kn winds, and mostly clear skies. Many crab pots in the area made maneuvering challenging. Matchups were obtained for all three VIIRS overpasses.

- On March 9th, the entire coastal area from Seattle to Newport and out to 150 NM was predicted to be cloudy. The ship headed west from our 3/8/2023 location trying to catch the edge of the clear sky but could only make it 140 NM offshore since we were limited on how far we could go as we had to return to Newport by the morning of March 11th. Stations 20, 21, and 22 were sampled on the edge of the clearing but could not get far enough offshore to get into the clear, and no satellite matchups were obtained.

- The operation had to head south on March 10th to start heading towards Newport as the ship was too far away. Spotty clouds were covering 50% to 70 % of the sky everywhere with bands of clouds moving rapidly from west to east (Figure 6). Despite best efforts in trying to time sampling between rapidly propagating bands, a minimal number of VIIRS-SNPP matchups were observed, with only station 24 having a significant number of matches.

- As the ship had to head into the port of Newport by noon on March 11th, only two near-shore stations (27 and 28) were able to be occupied directly off the port from Newport. Good matchups were obtained for all three VIIRS sensors.

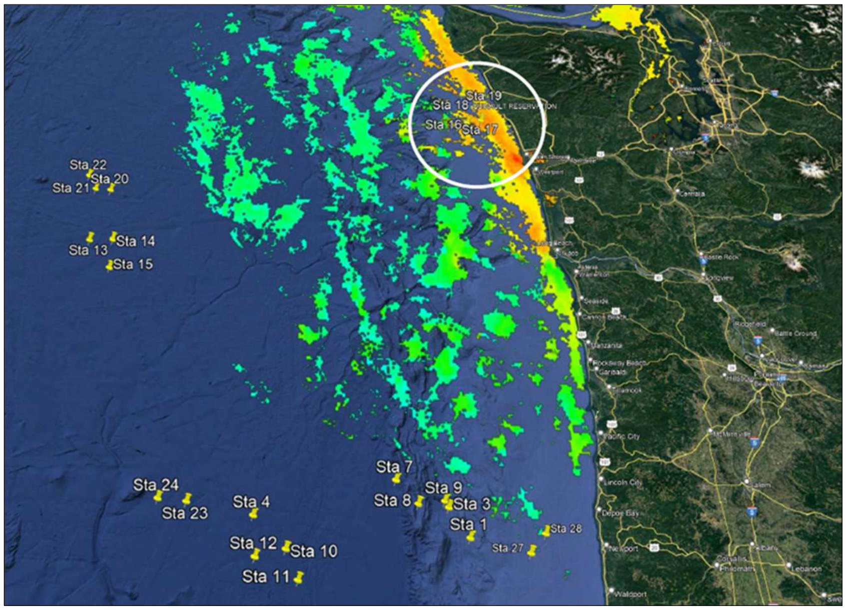


Figure 5. Satellite Chl-a image (March 8, 2023) showing stations 16, 17, 18, and 19.

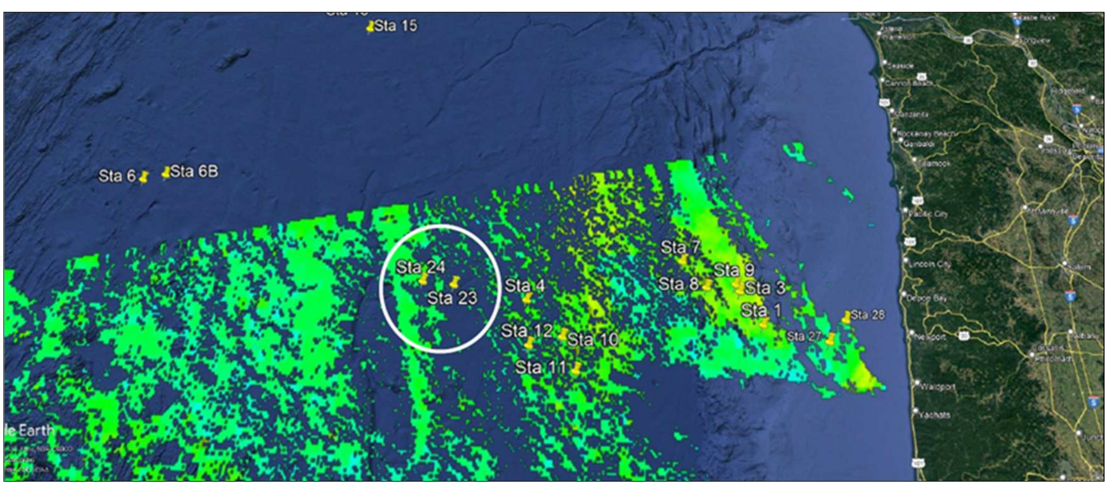


Figure 6. Satellite Chl-a image from March 10, 2023, when stations 23, 24, 25, and 26 were sampled.

# 3. Accomplishments by Individual Teams

## 3.1. NOAA/STAR Team – Michael Ondrusek, Menghua Wang, Eric Stengel, and Charles Kovach

NOAA/STAR, in addition to being responsible for cruise planning, organizing daily operations, station location planning, and liaison between the science party and the crew of *Bell M. Shimada*, also coordinated in-water and participated in above-water radiometric measurements of $R_{rs}$, which is the primary observation of this project.

### *3.1.1. Deployment of a radiometric profiler*

The profiler operated by NOAA/STAR was a Satlantic HyperPro-II profiling package with depth, temperature, and tilt sensors. The profiler (serial # 179) was equipped with one ECO-Puck sensor (SATB2F1492) that measured fluorescence and backscattering to estimate Chl-a concentrations and backscattering coefficient ($b_b$) at 470 nm and 532 nm. The profiler was also equipped with a downward-looking Satlantic Hyperspectral Ocean Color Radiometer (HyperOCR) for radiance (serial # 416) and an upward-pointing Satlantic irradiance sensor (serial # 530). Downwelling surface irradiance was measured with a surface irradiance ($E_s$) sensor (serial # 531) mounted aboard the ship. The NOAA profiler was deployed simultaneously with the USF and OSU HyperPro's utilizing the multicast deployment method, where data is continuously logged while each instrument is profiled 3 to 5 times down to 15 meters (Figure 7). This was replicated for 3 to 5 casts at each station. More discussion of the methods can be found in earlier dedicated VIIRS Cal/Val cruise reports [*Ondrusek et al.*, 2015; 2016; *Ondrusek et al.*, 2017; *Ondrusek et al.*, 2019; *Ondrusek et al.*, 2021; *Ondrusek et al.*, 2022; *Ondrusek et al.*, 2024].

### *3.1.2. Deployment of a floating instrument*

NOAA deployed an HTSRB floating radiometry system. This system consisted of the NOAA #179 profiler outfitted with the #206 upwelling radiance ($L_u$) sensor and the #233 downwelling plane irradiance ($E_d$) sensor. The #234 irradiance $E_s$ sensor was also mounted aboard the ship. All the $E_s$ sensors for the HyperPro profilers and HTSRB were mounted on a 35-foot telescoping pole to avoid stray-light reflectance contamination from the ship (Figure 8).

### *3.1.3. Above-water radiance observation*

NOAA/STAR deployed two above-water handheld instruments during the cruise. One system was the ASD FieldSpec HandHeld2 and the other was the SVC 512i spectroradiometer. The ASD has a spectral range of 325 nm to 1075 nm and a spectral resolution of less than 3 nm. This unit was equipped with a built-in GPS and was equipped with fore-optics with a 10-degree field of view (FOV). The other system NOAA used was an SVC HR-512i. The NOAA HR-512i covers a spectral range of 350 nm to 1050 nm, a 3 nm spectral resolution, and an 8-degree FOV. Above-water validation measurements were conducted on the bow simultaneously with the other team members (see NRL section) while the floaters and profilers were deployed. The method of *Mueller* *et al.* [2003a] was utilized with a NOAA Spectralon® white plaque with a nominal reflectance of 0.99. The water and plaque measurements were conducted at an angle of 40 to 45° from the nadir and an azimuth angle to the sun of 90° to 135°. The sky was measured at a 40 ° to 45° zenith angle and at an azimuth angle to the sun of 90° to 135°.

Figure 7. Simultaneous deployment of HyperPro profilers during SH-23-02. Top: Michael Ondrusek in the center deploying the NOAA HyperPro and Alex Bailess on the left (starboard quarter) deploying the OSU HyperPro. Bottom: a rogue wave revealing the difficult conditions during this project.

Figure 8. $E_s$ sensors mounted atop of telescoping pole at the upper structure of NOAA Ship *Bell M. Shimada.*

### *3.1.4. Aerosol measurements*

Aerosol optical thickness (AOT) was measured at 11 stations using a Microtops sunphotometer. The data are delivered for processing to NASA as part of the Aerosol Robotic Network (AERONET) program.

## 3.2. NRL Team – Sherwin Ladner

NRL collected above-water $R_{rs}(\lambda)$ measurements aboard *Bell M. Shimada* at 24 of the 28 station locations during March 2–11, 2023 using two handheld hyperspectral radiometers represented by white circles in Figure 9. Stations were adaptively planned and selected based on predicted (https://www.windy.com) weather forecasts and clear sky conditions to increase the probability of obtaining satellite matchups. NRL provided individual daily near-real-time Google Earth chlorophyll-a images for VIIRS sensors (SNPP and NOAA-20) in near real-time to assist in planning the next day's station locations and to determine if daily stations collected yielded valid sensor matchups.

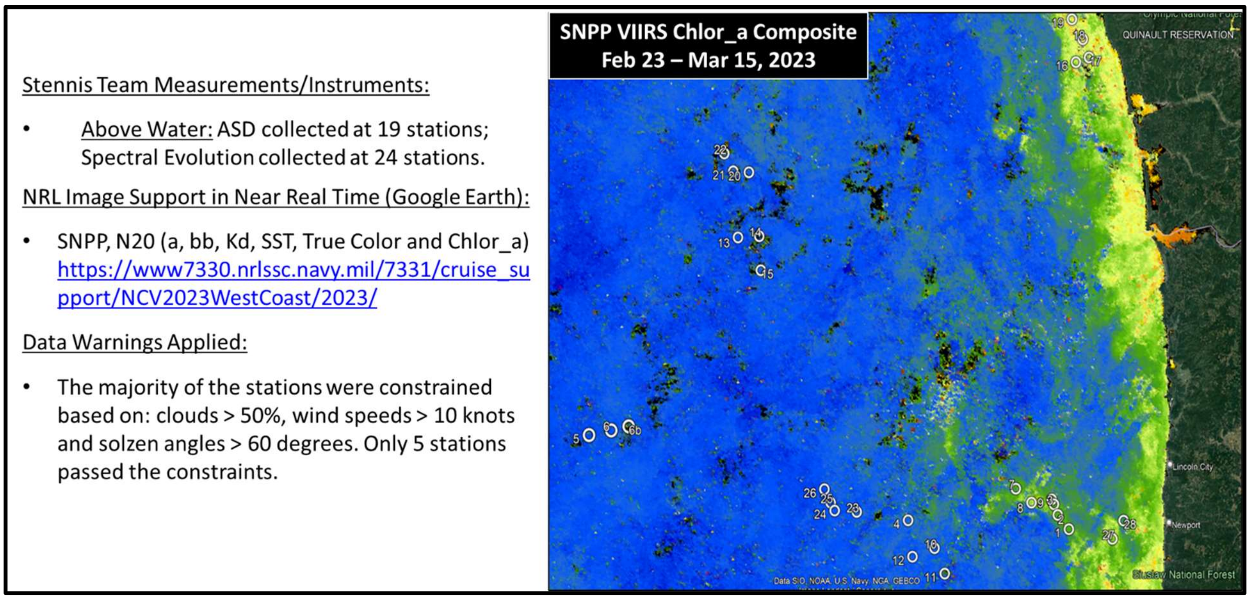


Figure 9. (Left) NRL measurements and assistance during the cruise. (Right) SNPP chlorophyll-a composite from February 23 to March 15, 2023, illustrating the 28 station locations covered aboard the NOAA Ship *Bell M. Shimada* out of Newport, Oregon. NRL's Automated Processing System v22 (APS) processed the individual daily and composite images. Vicarious calibration of all NOAA VIIRS sensors is performed annually at the ocean color standard calibration site MOBY in Hawaii.

### *3.2.1. Above-water radiometry measurements*

Above-water remote sensing reflectance measurements were taken using an ASD FieldSpec Handheld-2 hyperspectral spectroradiometer and an SEI PSR-1100F hyperspectral spectroradiometer. Each spectroradiometer was calibrated for spectral radiance using NIST-traceable standards by the respective manufacturers. The bow location was selected for collection to reduce the amount of contamination from the ship's structure on the collection of the calibrated reference plaque and the water's surface.

Above water measurements were acquired using the ASD (19 stations) and SEI (24 stations) spectroradiometers. All above-water measurements were made using the NRL white 99%

reflectivity 10-inch plaque during the standard sky, water, and reference plaque sequence for deriving the above-water $R_{rs}(\lambda)$. The white plaque has a known bidirectional reflectance distribution function (BRDF) surface and is used to normalize the uncalibrated irradiance measurements for $E_s$. Above-water measurements may vary due to instrument type and calibration, warm-up time, shadowing of the plaques, variable light field, etc.

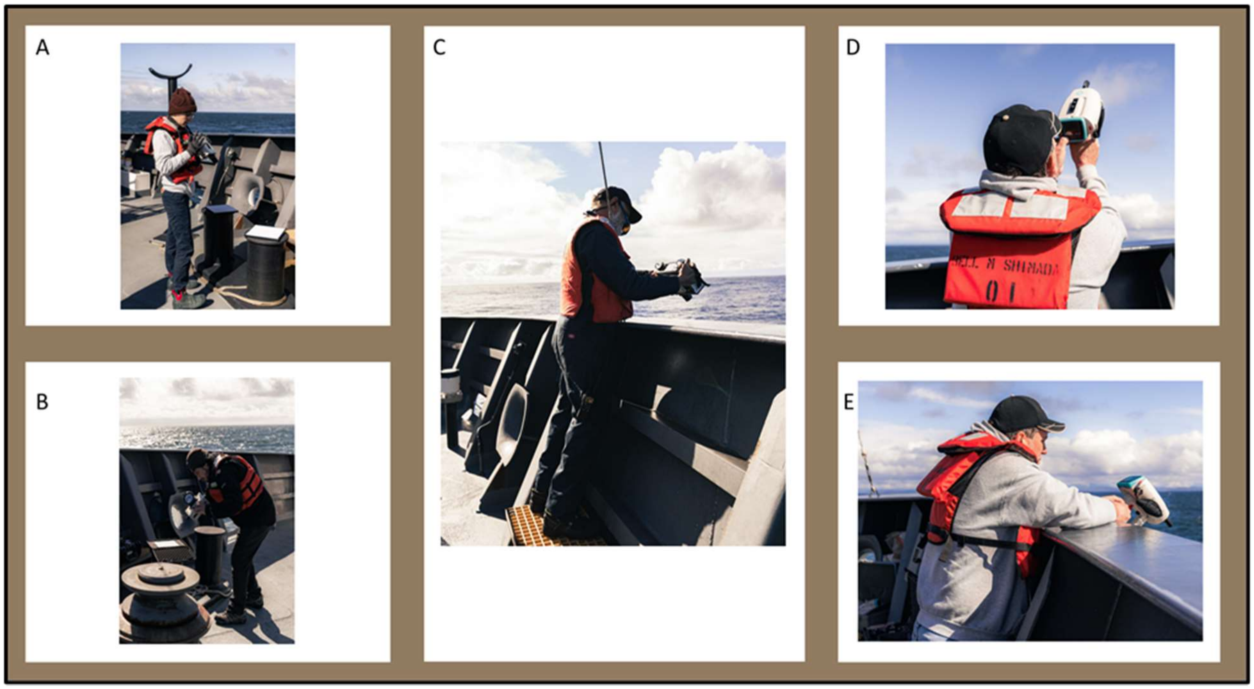


Figure 10. Illustrates the station collection sequence for above water $R_{rs}$. (A) Sarah Sullivan (USF) collecting the NRL 10-inch white reference plaque sequence with the USF SVC radiometer. (B) Eder Herrera (CCNY) collecting the CCNY 8-inch white reference plaque sequence with the CCNY SVC radiometer and (C) Charles Kovach (NOAA) collecting the above-water water sequence with the NOAA SVC radiometer. (D) Sherwin Ladner (NRL) collecting the sky irradiance sequence with the NRL ASD radiometer. (E) Sherwin Ladner (NRL) collecting the above-water sequence with the NRL ASD radiometer.

The above-water measurement activities took place on the bow of *Bell M. Shimada*. At the start of each station, the reference plaque was placed on the bow's bollard posts (Figure 10). The plaque was occasionally partially obscured from the full hemisphere by the ship's bridge, participants, cloud cover, and the bow rail at low sun angles (early morning and late afternoon). The magnitude of this bias will depend on how much of the diffuse component is blocked. Optimal and non-variable light conditions were sought for the sky, water, and reference measurements for the complete sequence. This was difficult due to the substandard weather conditions (high wind and cloudy conditions). NRL recorded station metadata (time, latitude, longitude, instrument base filenames, spectra target assignments and number of scans, ocean parameters from ship's flow-through, physical water characteristics, meteorology, etc.) on handwritten log sheets during each station and later compiled into an Excel spreadsheet by Charles Kovach (NOAA). Other personnel took photographs of the sky and water surface conditions and the participants in action. All groups in attendance attempted to make concurrent measurements using multiple above- water spectroradiometers while the profiling radiometers (HyperPro's) were being deployed. At the end of each station, the plaque was stored in its case, and instruments were powered off and placed in a watertight storage box on the bow. At the end of each day, they were taken back into the lab to download data and stored in their respective cases.

The NRL ASD instrument was configured to average 5 spectra per scan and save five spectra scans for each of the 3 targets (sky, reference, and water). The SEI is designed to collect one spectrum at a time and has to be triggered for each scan (10 scans per target). During each station, five consecutive radiometric spectra with dark measurements subtracted were taken of each of the following targets: 1) sky, 2) NRL white plaque, and 3) water for the ASD. The same sequence was collected for the SEI with 10 radiometric spectra per target. For both the ASD and SEI instruments, an 8-degree fore optic was attached, and the integration time was optimized for each target before collection (i.e., the integration time of the sensor was changed based on the relative brightness of the target and new dark counts were taken to correct for instrument noise). The sensor zenith angles for the $\theta_p$, $\theta_{sfc}$, and $\theta_{sky}$ measurements were 40°, 40° and 40°, respectively. The relative azimuth angle of the sensor to the sun ranged from 90° to 135° depending on visual surface contamination (sea foam, glint, bubble, shadows, etc.). The post-processing of the ASD and SEI above-water data collected by NRL was performed using code developed by NRL for the 24 stations collected and $R_{rs}(\lambda)$ was computed using the NRL white plaque using the same collection protocols for both instruments to look at the inter-sensor differences. The NRL software corrected the $R_{rs}(\lambda)$ using a NIR baseline-subtraction protocol and the calculation of the surface reflectance correction $\rho$, based on the solar azimuth and wind speed ($W_s$) calculation [*Mobley*, 2015]. This approach is a substantial improvement over using a constant $\rho$ of 0.021 to minimize the reflected sunlight contribution.

### *3.2.2. Above-water processing*

The ASD spectroradiometer measures light at 1.0 nm sampling over the 325 nm to 1075 nm spectral range. The SEI spectroradiometer measures light at 1.0 nm sampling over the 320 nm to 1100 nm spectral range. Processing follows the equation:

$$R_{rs}(\lambda) = (S_{w+s} - S_{sky}\,\rho(\theta))/(\pi S_p/refl) \tag{1}$$

where:

- $S_{w+s}$ is the measured signal from the water and includes both $L_w$ and reflected skylight;
- $S_{sky}$ is the measured signal from the sky;
- $S_p$ is the average measured signal from the white Spectralon® plaque;
- *refl* is the reflectivity of the plaque (approximately 99% white; actual measured spectral values are used in the calculation); and
- $\pi(\rho)$ converts the reflected radiance values to irradiance for these "Lambertian" diffusers.
- The measured sky radiance is multiplied by $\rho(\theta)$ which is the proportionality factor that relates the radiance measured when the detector views the sky to the reflected sky radiance measured when the detector views the sea surface.

The value of $\rho(\theta)$ is dependent on wind speed and direction, detector FOV, and sky radiance distribution. Only in the case of a level sea surface and a uniform sky radiance distribution does $\rho(\theta)$ equal the average of the Fresnel reflectance over the detector FOV. For our measurement angles under nominal sky and wind conditions, we pull $\rho(\theta)$ from the table of *Mobley* [2015].

The computed $R_{rs}(\lambda)$ is assumed to be "black" at about 750 nm due to water absorption. If not zero, then it is assumed that the $S_{sky}$ was not estimated correctly. Following the "quick and easy" algorithm [*Carder and Steward*, 1985], it is further assumed that any error in the skylight reflection term is white (not wavelength dependent) and one may simply subtract the computed $R_{rs}(750)$ from the entire spectrum. In practice, this may lead to negative reflectance values $R_{rs}(\lambda)$ near 750 nm. Therefore, the processing subtracts the smallest $R_{rs}(\lambda)$ in the range from 700 nm to 800 nm.

### 3.3. CCNY Team – Alex Gilerson, Eder Herrera, and Mateusz Malinowski

The main instrument of the CCNY group used for above-water observations in the validation process was a GER 1500. Measurements were also made with the hyperspectral polarimetric imaging system, which included snapshot hyperspectral imager ULTRIS X20 (Cubert, Germany) and polarization camera M2450 (Teledyne DALSA, Canada). In addition, AOT was measured by Microtops II sunphotometer (Solar Light, PA) at 5 wavelengths: 380, 500, 675, 870, and 1020 nm.

#### *3.3.1. Handheld spectroradiometer*

The GER 1500, Field Portable Spectroradiometer, is a hand-held spectroradiometer designed to provide fast spectral measurements covering the ultraviolet (UV), visible, and NIR wavelengths from 350 to 1050 nm at 3 nm full-width at half maximum (FWHM) resolution. It uses a diffraction grating with a silicon diode array that has 512 discrete detectors and provides the capacity to read 512 spectral bands. Subsequent download and analysis are done using a personal computer with a standard RS232 serial port and the GER 1500 licensed operating software. The GER 1500 is equipped and operated with a standard lens with 4° nominal FOV for above-water observations. The GER 1500 is used in the field to calculate $R_{rs}(\lambda)$ by measuring the total radiance ($L_t$) above the sea surface, the sky radiance ($L_s$), and the downwelling radiance ($L_d$).

The instrument underwent radiometric and wavelength calibration in the optics mode (with the lens) at the manufacturer in March 2019 with additional tests at CCNY. Generally, due to the nature of the measurement, calibration is not necessary. The main details of the data processing follow the Mobley 99 approach [*Mobley*, 1999] and are available in cruise report #4 [*Ondrusek et al.*, 2019].

#### *3.3.2. Hyperspectral polarimetric imaging system*

The system (Figure 11) included a snapshot hyperspectral imager with a manually rotatable polarizer and a polarization camera, with a filter wheel, which contained color filters. The system was operated by two laptop computers.

#### *3.3.3. Hyperspectral imager*

The imager has the unique capability of simultaneously recording data from 410×410 pixels, FOV = 35° in the hyperspectral mode for each pixel with 164 bands in the range of 350–1000 nm. It is used for measurements of radiances at various viewing and azimuth angles in the FOV and estimation of radiance uncertainties in the hyperspectral mode.

#### *3.3.4. Polarization camera*

Recently released Sony image polarization sensor with 2464 (H) × 2056 (V) pixels, where each 2×2 pixel area consists of four subpixels that are equipped with polarizers oriented at 0°, 90°, 45°, and −45°, respectively, was integrated by the Teledyne DALSA into M2450 camera and calibrated at CCNY. In our implementation, it is combined with a lens and a filter wheel (Finger Lakes Instrumentation, NY) containing five color band-pass filters (AVR Optics, NY) with rectangular transmission spectra at the following center wavelengths (bandwidths): 442 (42), 494 (41), 550 (32), 655(40), and 684 (24) nm, and one window without filter and measurements in the panchromatic mode. The camera and lens provide a rectangular FOV (HFOV × VFOV = 29.2° x 38.4°) similar to the FOV of the imager. Typical integration time was 2 ms for water measurements, 0.7 ms for sky measurements, and 0.05 ms for white plaque measurements. Videos of the water surface were acquired with a typical frame rate of about 30–40 frames/second and 8-bit digitization, standalone images were acquired with 8- and 12-bit digitization. The user interface provided by the manufacturer was integrated with the filter wheel interface to allow for the automatic acquisition of videos and images of polarization components. These images and videos were then reprocessed to get images and videos of Stokes vector components, the degree of linear polarization (DoLP), and the angle of linear polarization (AoLP), which are further used in the analysis [*Malinowski et al.*, 2023].

Polarimetric measurements provide important information in the characterization of ocean wave slopes [*Zappa et al.*, 2008] and analysis of their variability in different open ocean and coastal areas as a function of wind speed in comparison with the Cox-Munk model [*Cox and Munk*, 1954], which is in the atmospheric correction model.

Examples of comparison of measurements by GER and satellites for four stations are shown in Figure 12. GER spectra were adjusted to have $R_{rs}$ = 0 sr$^{-1}$ at 750 nm. There was a small number of matchups between in situ and satellite data in the cruise due to the rough sea and inclement weather, which also affected the quality of matchups.

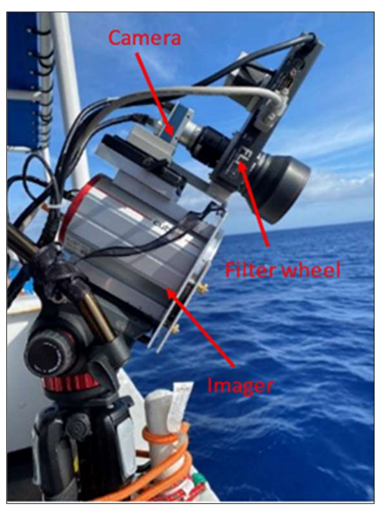


Figure 11. Snapshot hyperspectral imager with polarization camera on the ship.

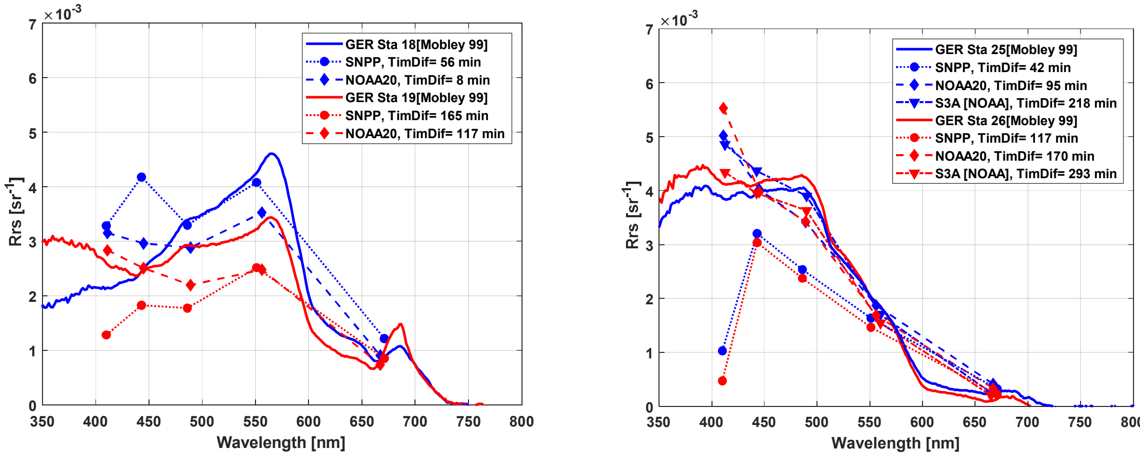


Figure 12. Comparison of measured spectra by GER and satellite data for several stations.

An example of the hyperspectral image data from one of the stations is shown in Figure 13. Standard deviation spectra are typical for windy conditions with some glint.

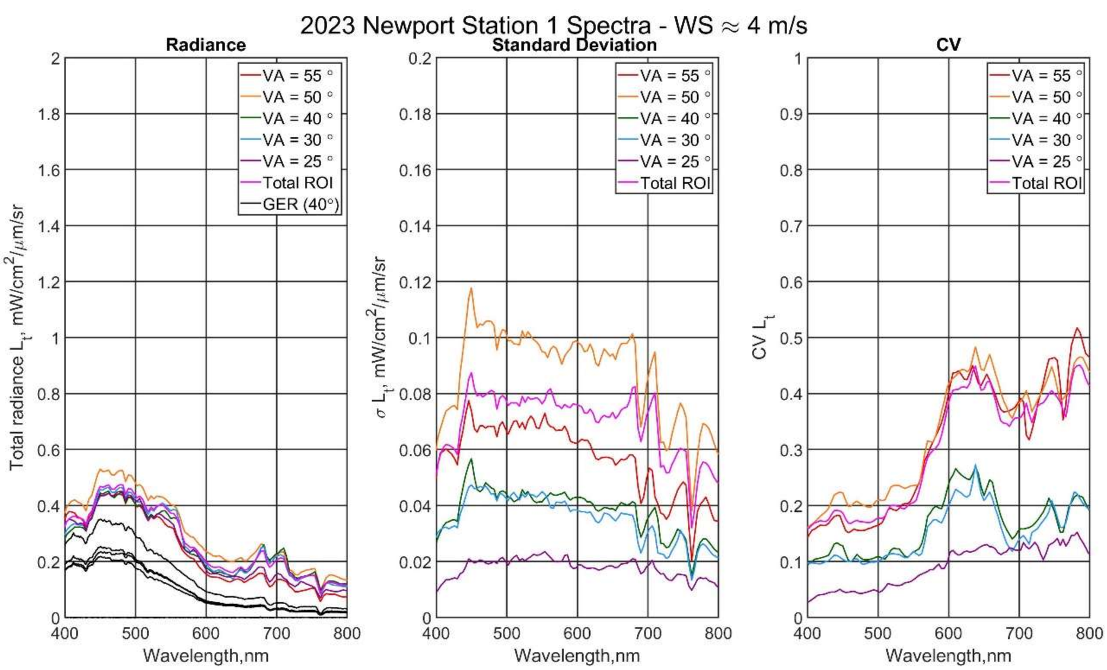


Figure 13. Data from the hyperspectral imager: above-water spectral radiances at viewing angles 25°–55° compared with GER spectra (left), radiances uncertainties (center), coefficient of variation or CV (right).

Examples of the estimation of wave slope variances using polarimetric sensing [*Zappa et al.*, 2008] with a modified algorithm [*Malinowski et al.*, 2024a] at 3 different bands and the comparison with Cox-Munk variances are shown in Figure 14. Slope variances obviously should not depend on the band and such small dependence is visible in Figure 14 with variances close to Cox-Munk variances.

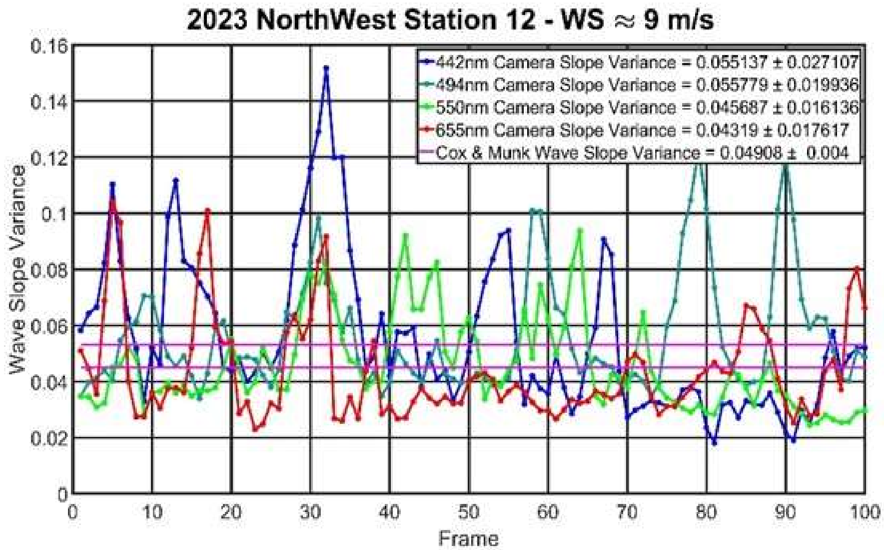


Figure 14. Estimation of wave slope variances using polarimetric sensing at Station 12.

Based on the analysis of data from several stations in the cruise using the modified polarimetric sensing technique the relationship between mean square slope (mss) variances and wind speed was established for the cruise as shown in Figure 15, which matched well the Cox-Munk relationship[*Cox and Munk*, 1954][*Cox and Munk*, 1954][*Cox and Munk*, 1954][*Cox and Munk*, 1954][*Cox and Munk*, 1954][*Cox and Munk*, 1954]. This work was further expanded to three VIIRS Cal/Val cruises, including the Gulf of America in 2021, Hawaii in 2022, and the U.S. west coastal oceans in 2023 [*Malinowski et al.*, 2024a]. Data from the imager and the camera for these cruises were also used for the estimation of radiometric uncertainties in above-water observations [*Malinowski et al.*, 2024b].

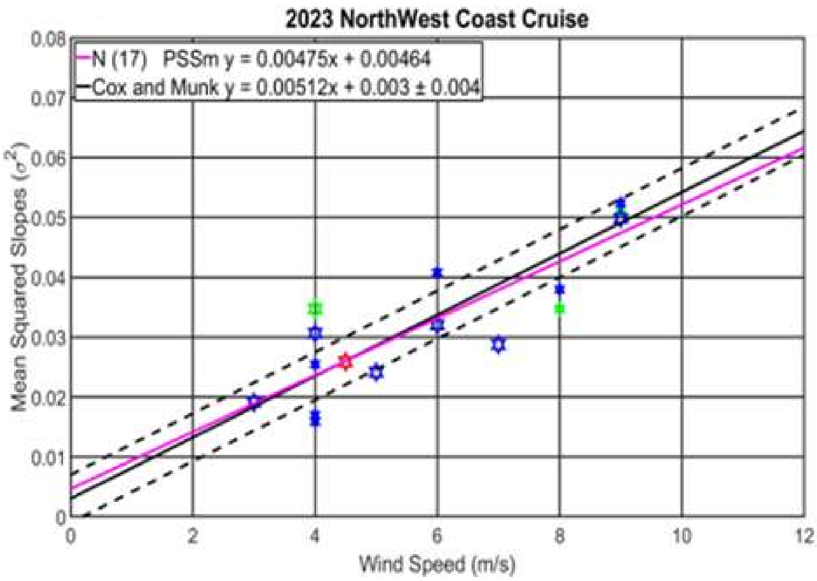


Figure 15. The camera recorded mean square slopes vs. wind speed for the 2023 cruise. The colors represent which color filter 442 nm (blue), 494 nm (cyan), 550 nm (green), or 655 nm (red) was selected. The corresponding sun zenith angle is shown by filled markers (around noon time) zenith with the angle at 25 to 35° and empty markers (morning and evening) with angles greater than 35°.

## 3.4. LDEO Team – Joaquim I. Goes and Helga do Rosario Gomes

The LDEO field team undertook high-resolution measurements of Chl-a, phytoplankton functional types (PFTs), phytoplankton size classes, and phytoplankton photosynthetic efficiencies in near-surface (~5 m) seawater samples that were pumped continuously through *Bell M. Shimada*'s uncontaminated seawater flow-through system. These measurements were repeated for discrete samples that were collected from three depths in the water column using a CTD rosette for a range of measurements as described below.

### *3.4.1. Discrete samples and measurements*

Water samples were collected from a total of 22 stations along the cruise track. Discrete seawater samples were obtained from 3 depths in the water column that were based on CTD fluorometric profiles. At each station, we sampled the water for the following:

i. Counting, imaging, and size estimations of phytoplankton and other detrital particles using Fluid Imaging Technologies, Inc., FlowCAM [*Jenkins et al.*, 2016].
ii. Estimates of phycobilipigments using a newly developed fluorescence technique developed at LDEO.
iii. Fluorescence-based estimates of Chl-a, colored dissolved organic matter (CDOM), open water cyanobacteria (OWCyan), coastal water cyanobacteria (CWCyan), cryptophytes (Crypto), and $F_v/F_m$, a measure of phytoplankton photosynthetic efficiency using a Custom Laser Spectrofluorometer (CLS) [*Chekalyuk and Hafez*, 2008; *Chekalyuk et al.*, 2012; *Goes et al.*, 2014].
iv. Measurements of photosynthetic quantum yields ($F_v/F_m$ ) [*Gorbunov and Falkowski*, 2004].

- FlowCAM-based phytoplankton identification, cell counts, and cell sizes

Subsamples (10 ml×2) aliquots of the preserved samples have been analyzed for phytoplankton community composition and size structure analysis using a FlowCAM particle imaging system equipped with a 4X objective (UPlan FLN, Olympus®) and a 300 µm FOV flow cell. FOV flow cells ensure that the liquid passing through the flow cell is entirely encompassed within the camera's field of view. Phytoplankton cells within the preserved samples have been counted and imaged in auto-image mode with a peristaltic pump rate of approximately 0.32 ml min$^{-1}$ to 0.44 ml min$^{-1}$ as specified by the manufacturer. Cells were classified to the genus level using the Visual Spreadsheet program (v. 2.2.2, Fluid Imaging). The instrument provides the total number of particles imaged, together with the dimensions of each particle allowing estimations of phytoplankton community structure and particle size distribution of both phytoplankton and detrital particles [*Goes et al.*, 2014; *Jenkins et al.*, 2016].

- Phycobilipigment collection and analysis

Approximately 1–2 liters of seawater samples from 2 depths were carefully filtered onto 4×25 mm Whatman GF/F filters for analysis of estimating phycoerythrin and phycourobilipigments. Samples were immediately stored in liquid nitrogen for later analysis at LDEO using methods developed by us which rely on freezing, sonication, and extraction of the phycobilipigments in phosphate buffer and analysis in a spectrofluorometer.

- Automated Laser Fluorescence (ALF) measurements of phytoplankton groups

The ALF combines high-resolution spectral measurements of blue (405 nm) and green (532 nm) laser-stimulated fluorescence with spectral deconvolution techniques to quantify the following:

All fluorescence values obtained are normalized to the Raman spectra of seawater and generally expressed as relative fluorescence units (RFU), whereas $F_v/F_m$ is unitless. PE-1 type pigments are associated with blue water or oligotrophic cyanobacteria with high phycourobilin/phycoerythrobilin (PUB/PEB) ratios, PE-2 type phytoplankton with low PUB/PEB ratios are generally associated with green water cyanobacteria that usually thrive in coastal mesohaline waters, and PE-3 attributable to eukaryotic photoautotrophic cryptophytes [*Chekalyuk and Hafez*, 2008; *Chekalyuk et al.*, 2012; *Goes et al.*, 2014].

RFU values for Chl-a can be converted into Chl-a values using least square regressions of acetone or High-performance liquid chromatography (HPLC)-measured Chl-a with RFU values for Chl-a measured in the CLS.

All samples for the ALF were collected directly from the Niskin samplers into 500 ml acid-washed amber glass bottles and stored for about 30 min in the dark at temperatures close to the average surface seawater temperature at each station. Dark adaptation allows all of the Photosystem II (PSII) reaction centers and electron acceptor molecules of phytoplankton to become fully oxidized and hence available for photochemistry thus minimizing the impacts of non-photochemical quenching before analysis.

### *3.4.2. Underway flow-through measurements*

Between stations, the CLS, the FlowCAM, and a Fluorescence Induction and Relaxation (FIRe) instrument were connected in parallel to the ship's seawater flow-through system, allowing for continuous in-water measurements of phytoplankton community composition, phytoplankton size, phycobilipigment types, and photosynthetic efficiency. Unfortunately, the lamp in the mini-FIRe suffered damage during shipment and the data collected was deemed as suspect and not shown here. Except for a few breaks during stations and for reconditioning, the CLS and FlowCAM were operated over the entire cruise track, providing several thousand fluorescence-based measurements of Chl-a, CDOM, PE-1, PE-2, PE-3, $F_v/F_m$, and $\sigma_{PSII}$, $p$ (a measure of electron transport between the PSII and PSI). Continuous flow-through measurements of phytoplankton species distribution and cell size distribution along the cruise track will provide useful information for interpreting the optical measurements for PFTs over the study area. The AlgaeOnlineAnalyser provides continuous measurements of Chl-a, plus the determination of cyanobacteria, green algae, brown algae (diatoms and dinoflagellates), and cryptophytes fluorescence using colored light-emitting diodes.

Data obtained with the flow through instrumentation allow us to obtain a synoptic picture of biological oceanographic conditions during the cruise (Figure 16a-c). Air and seawater temperatures were colder to the north as seen in the datasets collected during the northern transects diagonal to the coast. Waters sampled closer to the coast were much fresher than those offshore probably due to the influence of discharge from the Yaquina River on the southern transects and the influence of the Columbia River, and San Juan de Fuco Rivers along the northern transects (Figure 16a-c).

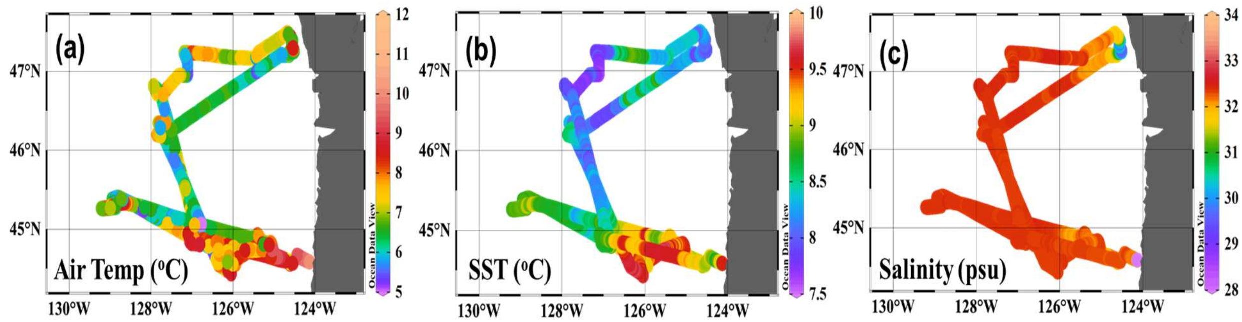


Figure 16. Distribution of a) Air temp b) SST, c) Salinity.

CLS-derived Chl-a concentrations (RFU) are shown in Figure 17a. Consistent with the satellite-derived Chl-a map, Chl-a concentrations were highest along the coastal region and distinct patches of high Chl-a observed along the cruise track were associated with coastal filaments moving offshore from the coast. The highest Chl-a concentrations were observed along the transect to the south where patches of high Chl-a were observed offshore in association with the offshore moving filament (Figure 17a). Values of variable fluorescence ($F_v/F_m$) with a few low-value patches, were high along the entire cruise transect and in particular in the high Chl-a regions (Figure 17b) indicative of actively photosynthesizing and growing phytoplankton populations. Surprisingly, CLS-derived CDOM values revealed lower CDOM values closer to the coast but higher in the patches of elevated Chl-a (Figure 17c).

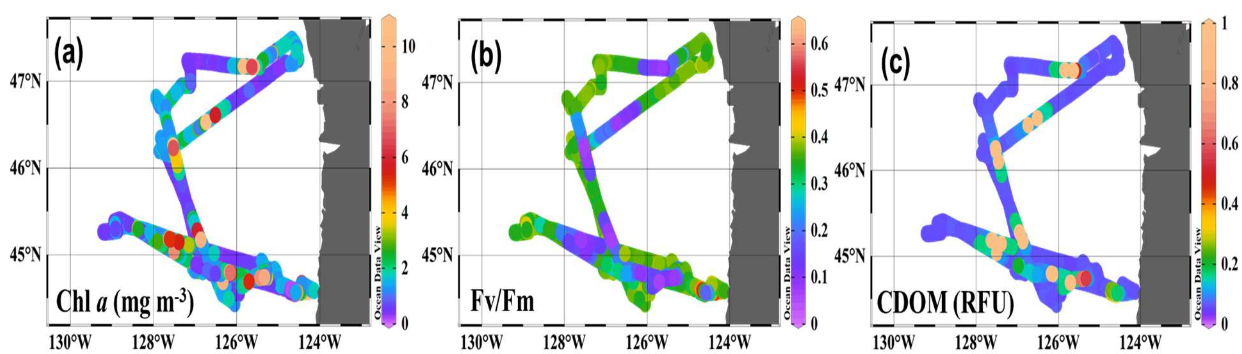


Figure 17. Distribution of CLS-derived a) Chl-a, b) Fv/Fm, and c) CDOM measured along the cruise track.

The distribution of BWCyan and CWCyan and Cryptophytes is shown in Figure 18a-c. BW Cyanobacterial concentrations were patchy along the entire cruise track, whereas CW

Cyanobacterial concentrations were higher on the southern leg. Cryptophyte concentrations were also relatively higher along the southern transects than the northern transects.

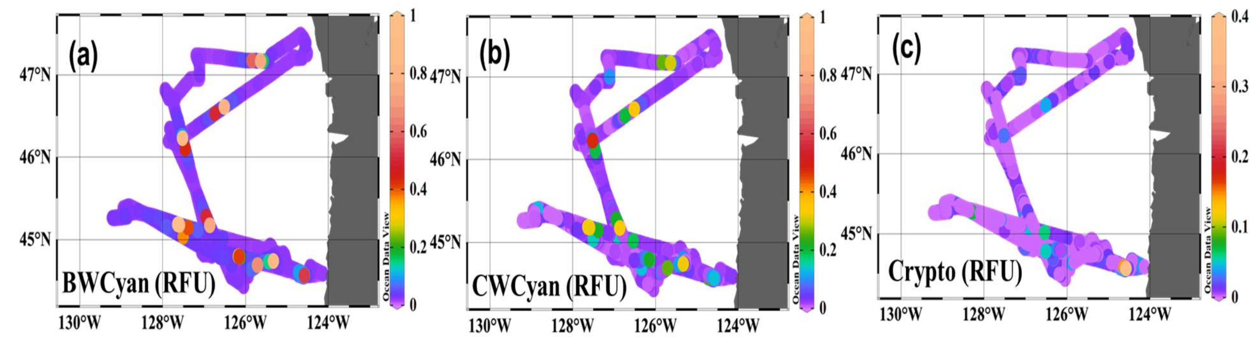


Figure 18. Distribution of a) Bluewater Cyanobacteria, b) Coastal water Cyanobacteria, and c) Cryptophytes.

Plots of dissolved $O_2$ and $pCO_2$ are consistent with CLS-derived fields of Chl-a and *Fv/Fm* in the regions of high Chl-a and high *Fv/Fm* (indicative of actively photosynthesizing populations) were regions where concentrations of dissolved $O_2$ were high and $pCO_2$ concentrations were low (Figure 19).

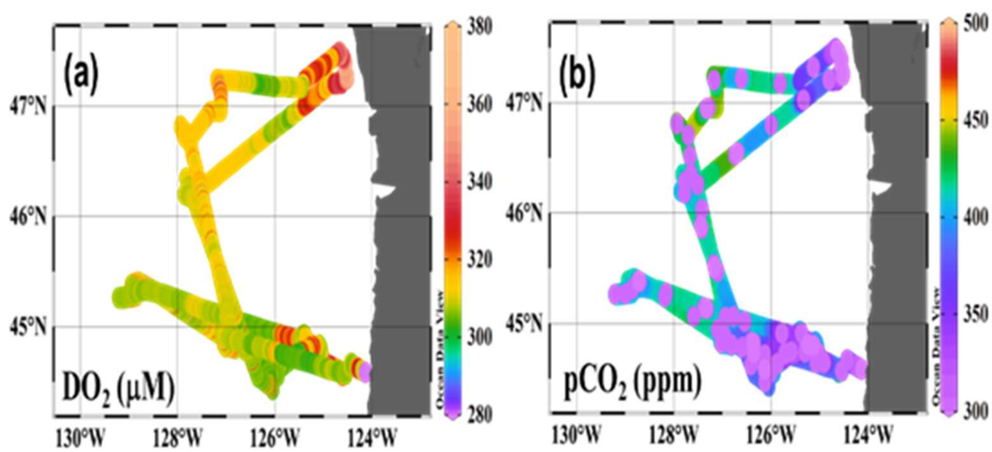


Figure 19. Dissolved $O_2$ and $pCO_2$ measured along the cruise track.

Chain-forming diatoms made up the bulk of the populations in the actively growing patches (Figure 20). At Station 1, the phytoplankton community was made up of *Astrioniella japonica, Thallasiosira* sp., and *Chaetoceros* sp., whereas Station 3 was dominated largely by mixotrophic dinoflagellates *Gyrodinium* sp. and *Gymnodiniod* sp. The chain-forming diatom *Chaetoceros* sp. made up the bulk of the population at Station 4. Station 11 which was sampled very close to Station 4 was also dominated by chain-forming *Chaetoceros* sp. Stations 13, 14, 21, and 22 located further northeast were dominated by a microzooplankton grazer population of tintinids. Stations 17–19 located close to the coast to the south of Seabrook, Washington were dominated by chain-forming diatoms, *Thallasionema* sp., *Astroniella* sp., *Thallasiosira* sp., and *Chaetoceros* sp. Station 23 located offshore was dominated by the diatom *Pseudo-nitzchia* sp., some of which are known to form toxic blooms.

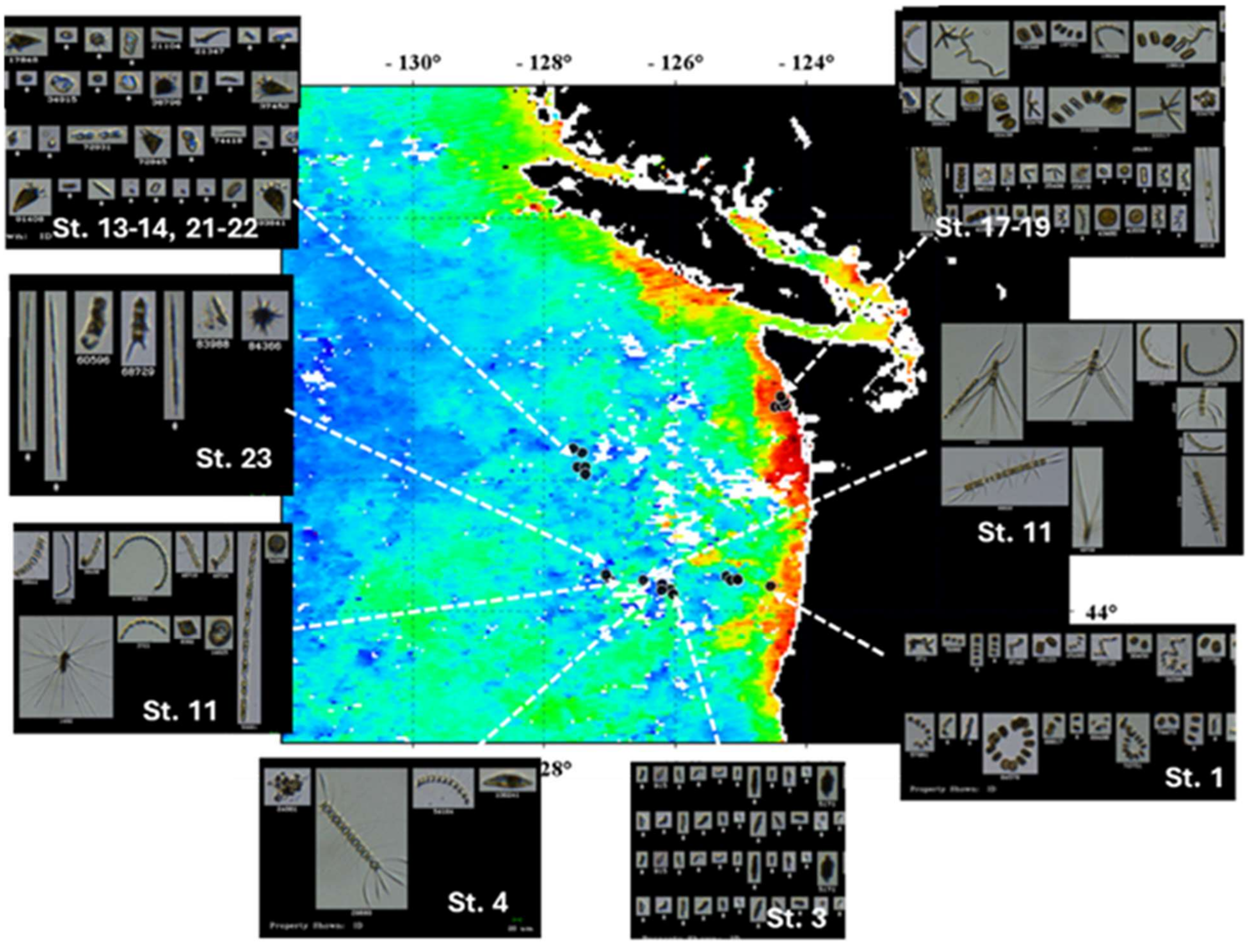


Figure 20. Distribution of major phytoplankton functional groups in the upper euphotic column during the Cal/Val cruise onboard *Bell M. Shimada.*

### 3.5. USF Team – Chuanmin Hu, Sarah Sullivan, Samuel Bunson, Jennifer Cannizzaro, and David English

During the 2023 Cal/Val cruise, water samples from the CTD rosette were filtered for later measurement of the spectral absorption of particulate and dissolved material, as well as the fluorometric determination of Chl-a. Additionally, a handheld spectroradiometer was used to collect sea-surface remote sensing reflectance measurements, and a HyperPro-II measured radiometric profiles during the cruise. These measurements provide estimates of both the spectral absorption of light from within the water and $R_{rs}(\lambda)$ (or $nL_w(\lambda)$) above the water surface.

#### *3.5.1. Spectral absorption and chlorophyll-a concentration*

Water samples from near-surface waters were collected using the CTD rosette at most stations, and from subsurface waters (> 15 m depth) at about half of these stations. The water sample was filtered through a glass fiber filter (Whatman® GF/F) and a portion of the filtrate was further filtered through a 0.2 µm polycarbonate filter and both the GF/F filters and filtrate were stored for later analysis. The shore-based measurement of the spectral light absorption of the filtrate allowed the determination of the CDOM absorption, $a_g(\lambda)$, while the absorption by particles in the water was derived from spectral measurements of the filters. The extraction of the particulate pigments during these measurements allows the separation of the total particulate absorption, $a_p(\lambda)$, into a pigmented fraction attributed to phytoplankton, $a_{ph}(\lambda)$, and detrital fraction, $a_d(\lambda)$ [*Kishino et al.*, 1985]. Additionally, the extraction of the pigments allowed fluorometric determination of the Chl-a concentration [*Holm-Hansen and Riemann*, 1978; *Welschmeyer*, 1994]. These Chl-a samples were processed using a Turner Trilogy fluorometer and the particulate absorption measurements were made using a Perkin Elmer Lambda 850+ spectrophotometer.

These samples were collected at 24 stations (Table 2) and subsurface samples (usually near 20 m depth) were collected at 12 of these stations. The Chl-a concentrations ranged from 0.5 to 6.9 mg $m^{-3}$ and averaged ~6 mg $m^{-3}$ near the coast and ~0.7 mg $m^{-3}$ offshore. The measurements of $a_g(400)$, which is an indicator of dissolved material, ranged from 0.03 to 0.12 $m^{-1}$ with values > 0.7 $m^{-1}$ only found at the first station off the Oregon coast and the 4 stations near the Washington coast. The absorption of both particulates and CDOM was greater than those measured in Hawaiian waters during the 2022 VIIRS Cal/Val cruise. Example spectral absorptions from the SH-23-02 cruise samples are shown in Figure 21.

#### *3.5.2. Above-water remote sensing reflectance*

Above-water $R_{rs}(\lambda)$ data were collected at 23 stations using an SVC HR-512i spectroradiometer. The $R_{rs}(\lambda)$ for each station is derived from multiple measurements of radiance from the water's surface, the sky, and a white-reference reflectance plaque [*Carder and Steward*, 1985; *Mueller et al.*, 2003b], and a correction for reflected skylight [*Mobley*, 1999] was applied. The measurements were made from a location near the ship's bow and the HR512i was configured with a 4° FOV fore-optic lens. The measurement was made viewing the sea surface and sky ($\theta_w$ & $\theta_s$) at approximately 40° from the nadir and zenith, respectively. The sea-surface viewing angle is recorded by the HR-512i for each measurement and was used to estimate the water's skylight reflectance value during the computation of the $R_{rs}(\lambda)$. Table 3 shows the measurement times and locations of the above-water $R_{rs}(\lambda)$ and HyperPro stations during the cruise and the above-water $R_{rs}(\lambda)$ spectra at each station are shown in Figure 22.

The persistent cloudy and windy conditions during the cruise increased the uncertainty of the above-water $R_{rs}(\lambda)$ measurements at almost all the stations, and the measurements at several stations were made at solar zenith angles greater than the maximum angle for reliable $R_{rs}(\lambda)$ derivation. Due to extensive cloud cover, high wind speeds, and rough sea states, the variability of $R_{rs}(\lambda)$ in the above-water measurement sequence was greater than those observed for stations of previous VIIRS Cal/Val cruises or the HyperPro-derived $R_{rs}(\lambda)$ of this cruise. While the $R_{rs}$ magnitudes were similar to those estimated from the HyperPro profiles for many of the stations, the blue portion of the above-water-derived $R_{rs}$ spectra frequently was lower than the HyperPro-derived spectra at stations measured at times of high solar-zenith angle. The above-water $R_{rs}(\lambda)$ is likely inaccurate due to the combination of inappropriate skylight correction factors at high $\theta_s$ and the variability of the sea surface orientation during rough seas and high winds. The $R_{rs}(\lambda)$ from above-water measurements during this cruise should be used with caution because cloudy conditions, $W_s > 10$ m s$^{-1}$, and/or $\theta_s > 60°$ were recorded during the majority of the above-water $R_{rs}(\lambda)$ stations as can be seen in Table 3.

### *3.5.3. In-water radiometry*

The USF Satlantic HyperPro-II was deployed within near-surface waters at 23 of the 28 cruise stations (Table 3). The HyperPro-II profiler included sensors measuring $L_u(\lambda,z)$, $E_d(\lambda,z)$, pressure, temperature, conductivity, $b_b(660)$, and both Chl-a and CDOM fluorescence. The HyperPro's data logging software, SatView, combined these measurements with above-water irradiance, $E_s(\lambda)$, and GPS data. The $L_u(\lambda,z)$, $E_d(\lambda,z)$, and $E_s(\lambda)$ measurements from multiple casts were used by the Satlantic Prosoft (v8.1.6) software to estimate radiance, irradiance, and reflectance (i.e., $L_w(\lambda,0^+)$ and $E_d(\lambda,0^+)$, $R_{rs}(\lambda)$, and $nL_w(\lambda)$) of the sea surface at each station. USF's HyperPro profiler was deployed using the manufacturer's recommended protocol in coordination with the other HyperPro profilers in use during the cruise. $R_{rs}(\lambda)$ estimates derived from the HyperPro-II profiles at each station are shown in Figure 23.

While the reliability of above-water $R_{rs}(\lambda)$ was diminished by the cloudy skies and increased wave heights due to windy conditions, the impact of these conditions on $R_{rs}(\lambda)$ generated from multiple HyperPro-II profiles should not be as severe. Consequently, the series of HyperPro-II profiles at each station provides a more robust $R_{rs}(\lambda)$ and $nL_w(\lambda)$ estimate than those derived from the above-water measurements in cloudy, windy conditions such as those present during this cruise.

Table 2. SH23-02 water sampling stations for light absorption measurements. A "●" indicates sample collection.

| SH23-02 Station | sample time (UTC) | Latitude (°) | Longitude (°) | surface sample | subsurface sample | subsurface depth (m) |
|---|---|---|---|---|---|---|
| 1 | 03/02/23 20:25 | 44.642 | -124.934 | ● | ● | 33 |
| 3 | 03/03/23 00:57 | 44.796 | -125.065 | ● | ● | 25 |
| 4 | 03/03/23 17:09 | 44.696 | -126.343 | ●* | ● | 20 |
| 6 | 03/04/23 21:54 | 45.282 | -128.988 | ● | | |
| 6b | 03/04/23 23:42 | 45.309 | -128.841 | ● | | |
| 7 | 03/05/23 17:30 | 44.912 | -125.374 | ● | ● | 20 |
| 8 | 03/05/23 21:30 | 44.805 | -125.293 | ● | | |
| 9 | 03/05/23 23:10 | 44.820 | -125.080 | ● | | |
| 10 | 03/06/23 17:00 | 44.567 | -126.134 | ● | | |
| 11 | 03/06/23 20:35 | 44.442 | -126.054 | ● | | |
| 12 | 03/07/23 01:15 | 44.546 | -126.346 | ● | | |
| 13 | 03/07/23 17:15 | 46.344 | -127.818 | ●* | ● | 20 |
| 14 | 03/07/23 19:46 | 46.347 | -127.620 | ● | ● | 15 |
| 15 | 03/08/23 01:10 | 46.162 | -127.623 | ● | | |
| 16 | 03/08/23 18:30 | 47.207 | -124.634 | ● | | |
| 17 | 03/08/23 20:30 | 47.256 | -124.515 | ● | | |
| 18 | 03/08/23 22:00 | 47.370 | -124.559 | ● | | |
| 19 | 03/09/23 00:01 | 47.477 | -124.654 | ● | | |
| 20 | 03/09/23 21:00 | 46.706 | -127.705 | ● | ● | 20 |
| 22 | 03/10/23 00:45 | 46.810 | -127.936 | ● | ● | 20 |
| 23 | 03/10/23 17:15 | 44.804 | -126.813 | ● | ● | 20 |
| 24 | 03/10/23 20:10 | 44.820 | -127.008 | ● | ● | 20 |
| 26 | 03/11/23 00:45 | 44.943 | -127.100 | ● | ● | 20 |
| 27 | 03/11/23 16:07 | 44.568 | -124.550 | ● | ● | 20 |

* CDOM only (filter sample missing)

Table 3. SH23-02 station times and locations for above-water $R_{rs}(\lambda)$ and HyperPro profile measurements. Except at station 16, the above water $R_{rs}(\lambda)$ and HyperPro measurements were conducted within 15 minutes of each other. A "●" indicates a HyperPro or above-water measurement was made at the stations, and indications of conditions that degrade the reliability of an above-water $R_{rs}$ are shown in the rightmost column.

| **Station** | **Sample time (UTC)** | **Latitude (°)** | **Longitude (°)** | **above-water $R_{rs}(\lambda)$** | **HyperPro** | **Adverse $R_{rs}$ conditions** |
|---|---|---|---|---|---|---|
| 1 | 3/2/2023 19:59 | 44.641 | -124.921 | | ● | C |
| 2 | 3/2/2023 22:28 | 44.730 | -125.032 | ● | ● | C |
| 3 | 3/3/2023 00:14 | 44.793 | -125.059 | ● | ● | S,W |
| 4 | 3/3/2023 17:09 | 44.696 | -125.343 | | ● | S,C |
| 5 | 3/3/2023 20:06 | 44.743 | -126.361 | | | W,C |
| 6 | 3/4/2023 22:26 | 45.288 | -129.000 | ● | | W,C |
| 7 | 3/5/2023 18:17 | 44.925 | -125.398 | ● | ● | S,C |
| 8 | 3/5/2023 20:13 | 44.809 | -125.263 | ● | ● | C |
| 9 | 3/5/2023 22:10 | 44.820 | -125.080 | | | W,C |
| 10 | 3/6/2023 18:10 | 44.582 | -126.136 | ●* | ● | C |
| 11 | 3/6/2023 20:04 | 44.435 | -126.051 | ● | | S |
| 12 | 3/6/2023 23:56 | 44.544 | -126.339 | ● | | S,C |
| 13 | 3/7/2023 18:12 | 46.347 | -127.825 | ● | ● | S |
| 14 | 3/7/2023 19:46 | 46.347 | -127.620 | | ● | C |
| 15 | 3/7/2023 23:59 | 46.157 | -127.618 | ● | ● | S,C |
| 16 | 3/8/2023 18:34 | 47.210 | -124.638 | ● | ● | |
| 17 | 3/8/2023 20:14 | 47.248 | -124.519 | ● | ● | |
| 18 | 3/8/2023 21:51 | 47.355 | -124.565 | ● | ● | W |
| 19 | 3/8/2023 23:48 | 47.475 | -124.652 | ● | ● | S,W |
| 20 | 3/9/2023 20:13 | 46.706 | -127.715 | ● | ● | C |
| 21 | 3/9/2023 22:25 | 46.716 | -127.858 | ● | ● | C |
| 22 | 3/9/2023 23:39 | 46.818 | -127.939 | ● | ● | S,C |
| 23 | 3/10/2023 18:01 | 44.805 | -126.816 | ●* | ● | C |
| 24 | 3/10/2023 20:54 | 44.818 | -127.014 | ● | ● | W,C |
| 25 | 3/10/2023 22:27 | 44.860 | -127.041 | ● | ● | |
| 26 | 3/10/2023 23:44 | 44.939 | -127.099 | ● | ● | S,C |
| 27 | 3/11/2023 17:14 | 44.571 | -124.549 | ●* | ● | S |
| 28 | 3/11/2023 18:31 | 44.664 | -124.436 | ●* | ● | |

●* indicates incomplete or excessively variable $R_{rs}$ measurement sequence.
C = skies had 50% or greater cloud cover; W = $W_s$ >10 m $s^{-1}$; S = $\theta_s$ >60°.

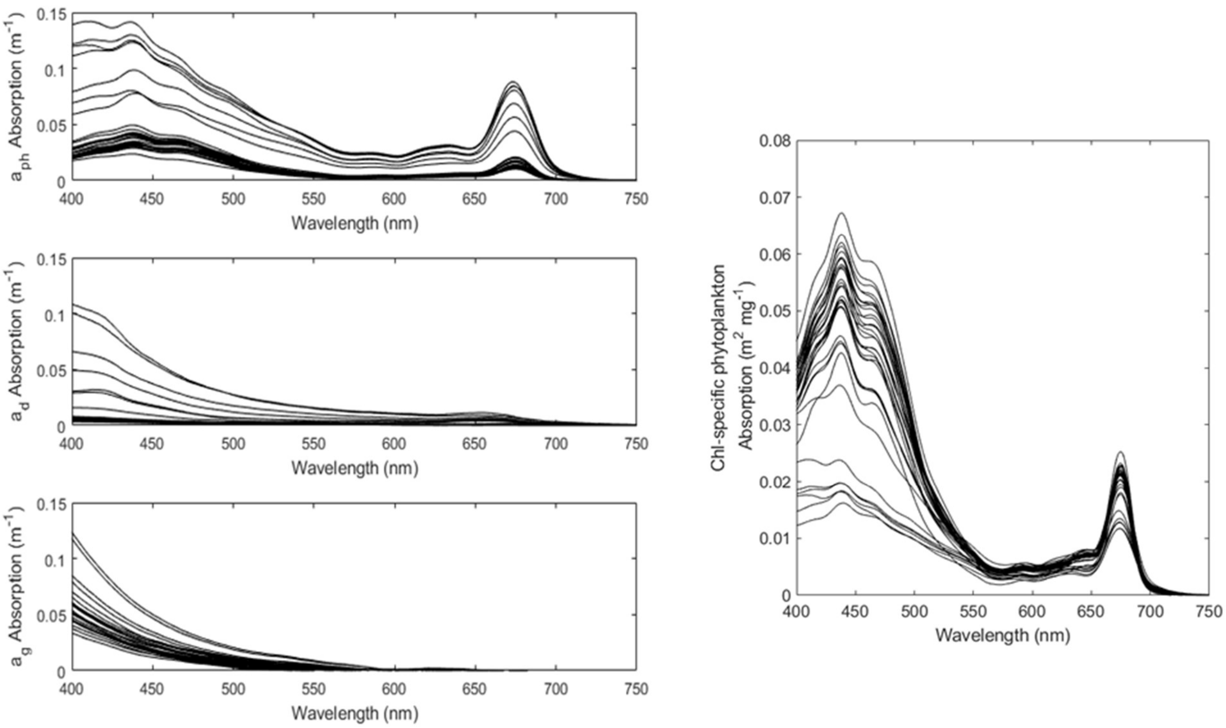


Figure 21. Spectral light absorption coefficients for phytoplankton pigments ($a_{ph}(\lambda)$, top-left), non-pigmented particulate matter or detritus ($a_d(\lambda)$, center-left), colored dissolved organic matter ($a_g(\lambda)$, bottom-left), and the chlorophyll-specific phytoplankton absorption ($a^*_{ph}(\lambda)$, right panel).

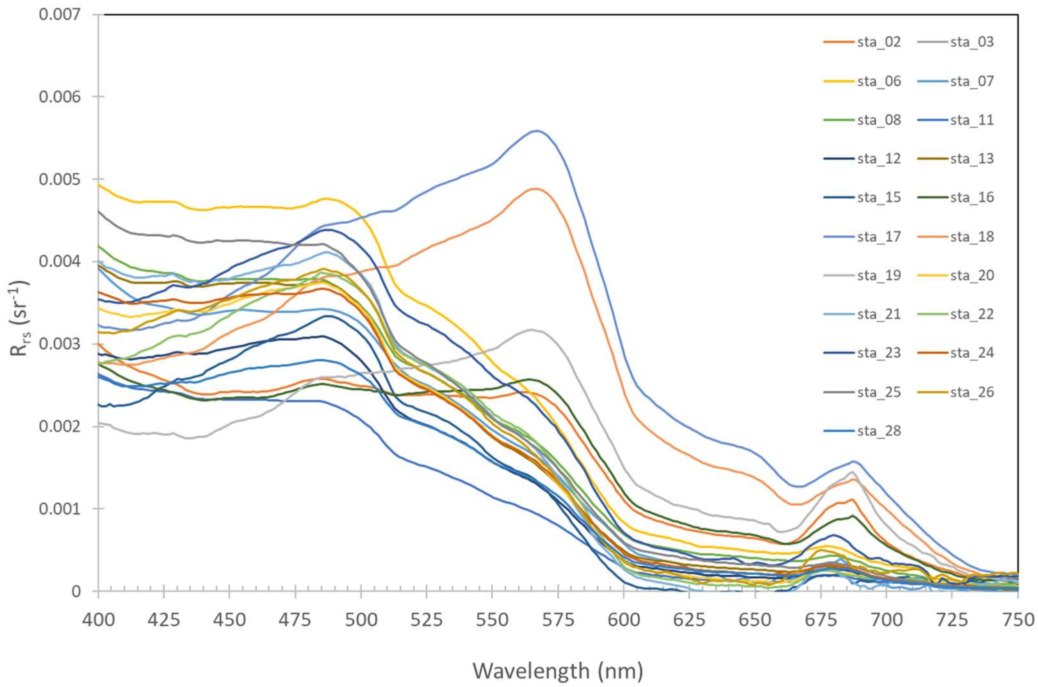


Figure 22. $R_{rs}(\lambda)$ derived from above-water SVC HR-512i measurements during SH23-02.

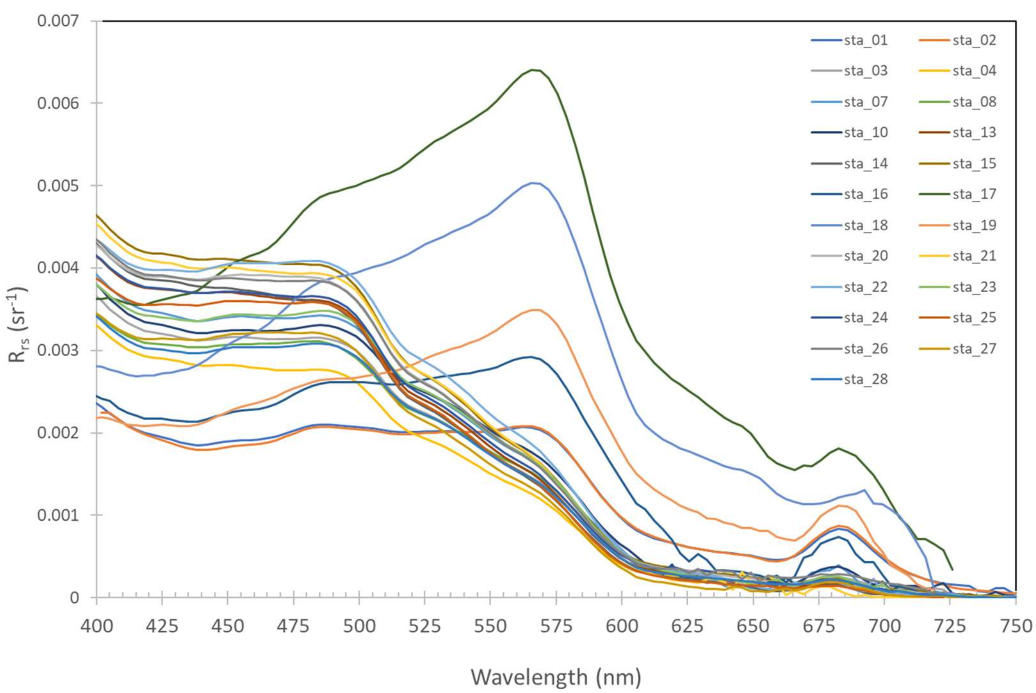


Figure 23. $R_{rs}(\lambda)$ estimated from HyperPro-II profiles at SH23-02 stations.

## 3.6. OSU Team – Wave Moretto, Jamon Jordan, Andrew Barnard, Maria Kavanaugh, Alexander Bailess, and Nick Tufillaro

The OSU team measured AOPs and IOPs of the northern California Current during the Cal/Val cruise. This was done using a hyperspectral in-water profiler, a hyperspectral above-water radiometer, and a suite of inline IOP sensors including a WET Labs AC-S instrument, and a BB3. OSU's main objective for this cruise was to derive water-leaving radiance and reflectance from the above- and in-water radiometers for inter-comparison and ocean color product validation for SNPP, NOAA-20, and NOAA-21.

### *3.6.1. Apparent optical properties*

OSU operated a series of hyperspectral ocean color sensors using the Satlantic HyperPro-II in the free-fall profiler configuration (Figure 24). An $E_s$ sensor was mounted to a pole on the ship with other $E_s$ sensors to reduce scattered light contamination from the vessel. A $L_u$ sensor and an $E_d$ sensor were mounted directly onto the HyperPro-II system in the standard configuration to derive $L_w(\lambda)$, $nL_w(\lambda)$, and $R_{rs}(\lambda)$. The HyperPro-II is also equipped with a WET Labs ECO Puck, measuring scattering at 470 nm and 700 nm and chlorophyll fluorescence at 470 nm and 695 nm.

The HyperPro-II was deployed overboard and kited away from the ship so that the shadow of the ship and other contaminating light effects from the vessel would not interfere with the optical measurements. As a rule of thumb, the HyperPro-II was kited at least 20 m away from the hull. We ensured that the $E_d$ sensor of the HyperPro-II was facing the sun to avoid self-shadowing during deployment. Weighting in the nose cone is configured for the ambient density to allow a 'slow drop' rate of ~0.3 m/s for adequate data collection.

Data was collected using Satlantic's SatView, and Nils Haentjen's (University of Maine), *Inlinino*, which is available at: [https://github.com/OceanOptics/Inlinino](https://github.com/OceanOptics/Inlinino). Recent updates of *Inlinino* are compatible with the deployment of the HyperPro-II system, and we favored this user interface to Satlantic's SatView. Post-processing was performed with Satlantic's ProSoft version 8.1.4 using protocols outlined by Oregon State University's standard protocols available for download ([http://aquahue.net/aquahue/papers/x_tec_hyperpro_processing.pdf](http://aquahue.net/aquahue/papers/x_tec_hyperpro_processing.pdf)). Data were also processed by the NOAA protocols developed by Mike Ondrusek. ProSoft used the following equation to derive the above-water products such as,

$$R_L(0^+,\lambda) = \frac{L_w(0^+,\lambda)}{E_d(0^+,\lambda)}, \quad (2)$$

where $E_d(0^+, \lambda)$ denotes the downwelling spectral irradiance measured just above the surface or extrapolated through the surface $E_d(0^+)$. $L_w(0^+, \lambda)$ denotes the upwelling spectral radiance propagated through the surface. For $E_s$ from the ship-based irradiance sensor, spectral bands are interpolated and matched to the in-water radiance sensor. Additional quantities such as $L_w(\lambda)$ and $R_{rs}(\lambda)$ are defined in the ProSoft manual.

Figure 24. Left is a constructed image of the HyperPro-II profiler system, consisting of the dart and wings (body) connected to two hyperspectral radiometers. Middle is a picture of the HyperPro-II being transported by Wave Moretto from the deck to the fantail for deployment. Right is the deployment of the HyperPro-II off the fantail.

An example of the in-water $L_u$ and $E_d$ is shown in Figure 25 for 488 nm to give a sense of the error distribution of the optical properties of offshore Oregon. Figure 25 displays a series of points at each depth, sometimes overlapping. This high density of measurements comes from several profiles (in this example, 3) of the instrument for each 'cast'. This multicast profiling facilitates better surface reflectance values by allowing us to average the effects of suboptimal tilt and wave focusing. This is a particularly good cast, a period of low wind and waves allowing for most data to pass the quality control for the tilt of the instrument (5º) and with relatively small changes in the underwater light field throughout the course of the profile from wave focusing.

One example of the water leaving radiance derived from the HyperPro-II profiler is shown in Figure 26. These water-leaving radiances are from the same profiles and images as above in Figure 25.

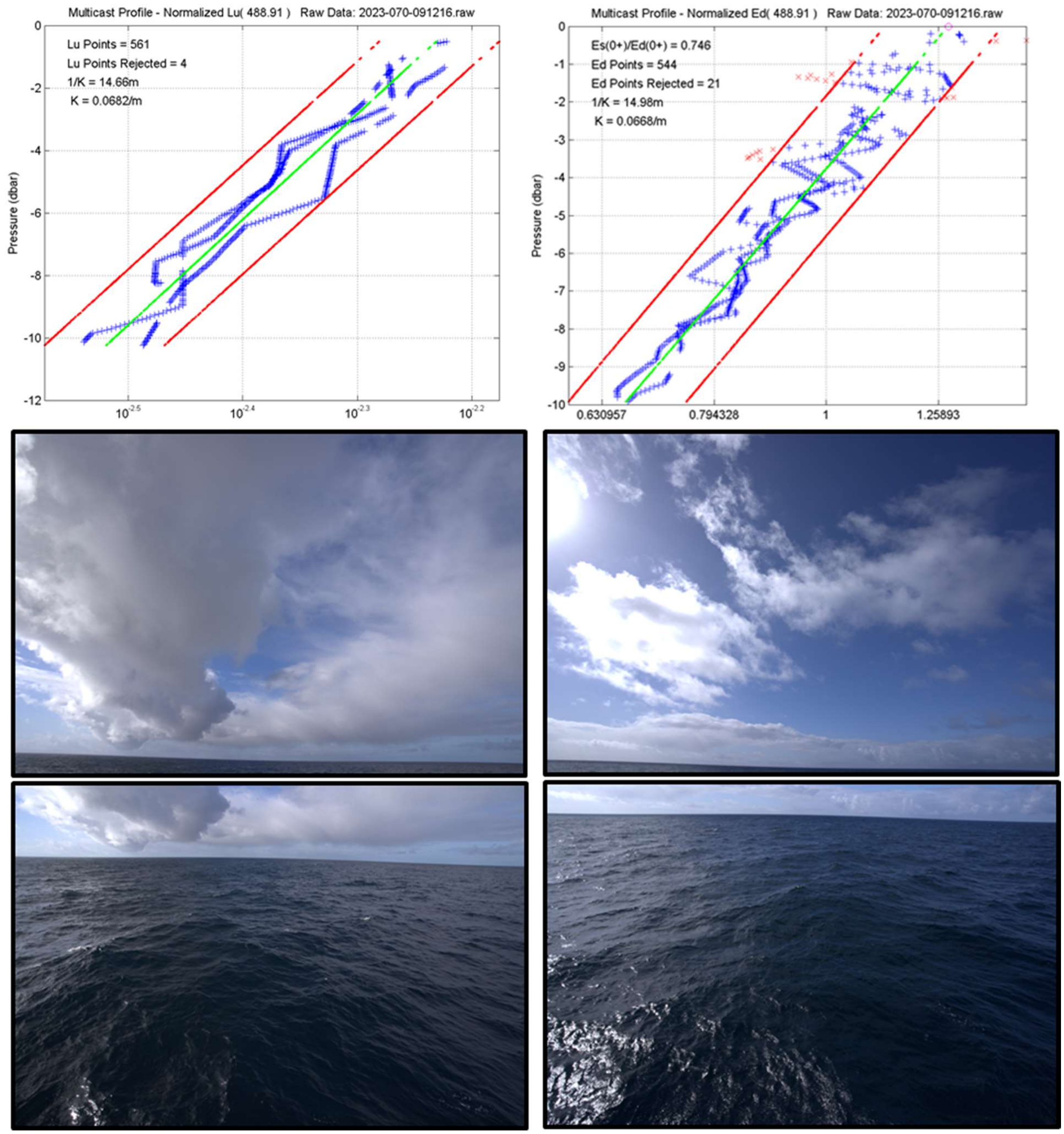


Figure 25. Examples of $L_u$ and $E_d$ profiles from the HyperPro-II for 488 nm and RGB pictures of the water in which the HyperPro's were deployed.

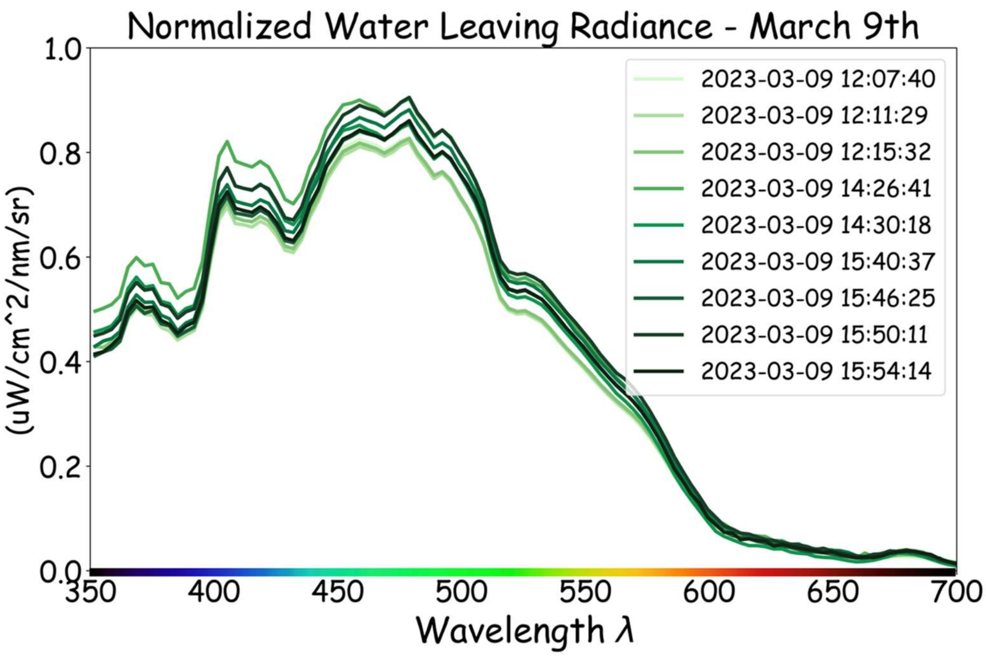


Figure 26. Example of water leaving radiance derived from OSU HyperPro-II for the 9th of March 2023.

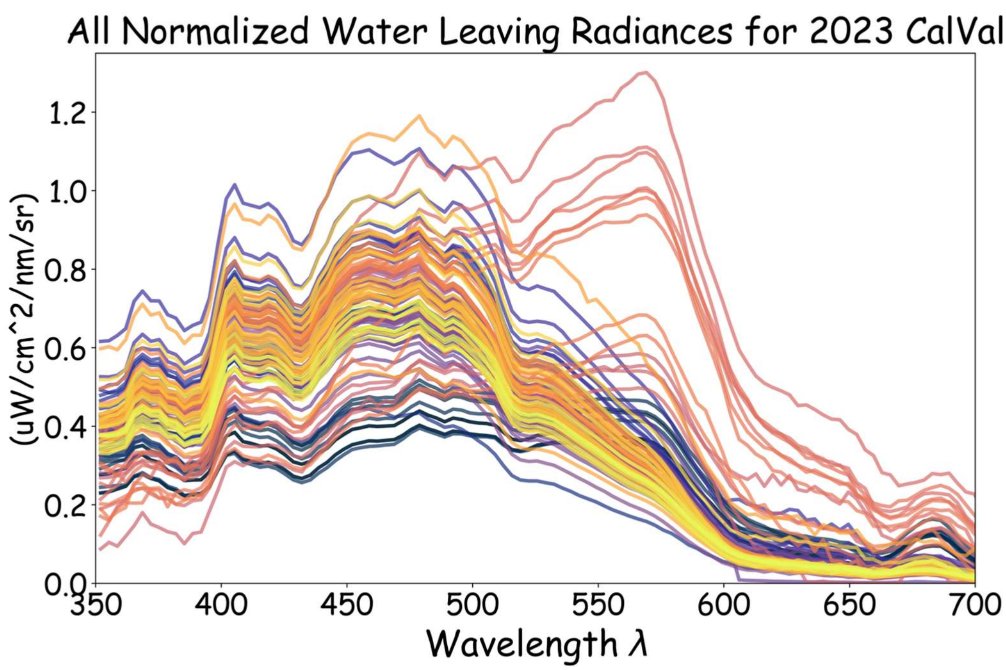


Figure 27. All water leaving radiance derived from the OSU HyperPro-II throughout the entirety of the cruise.

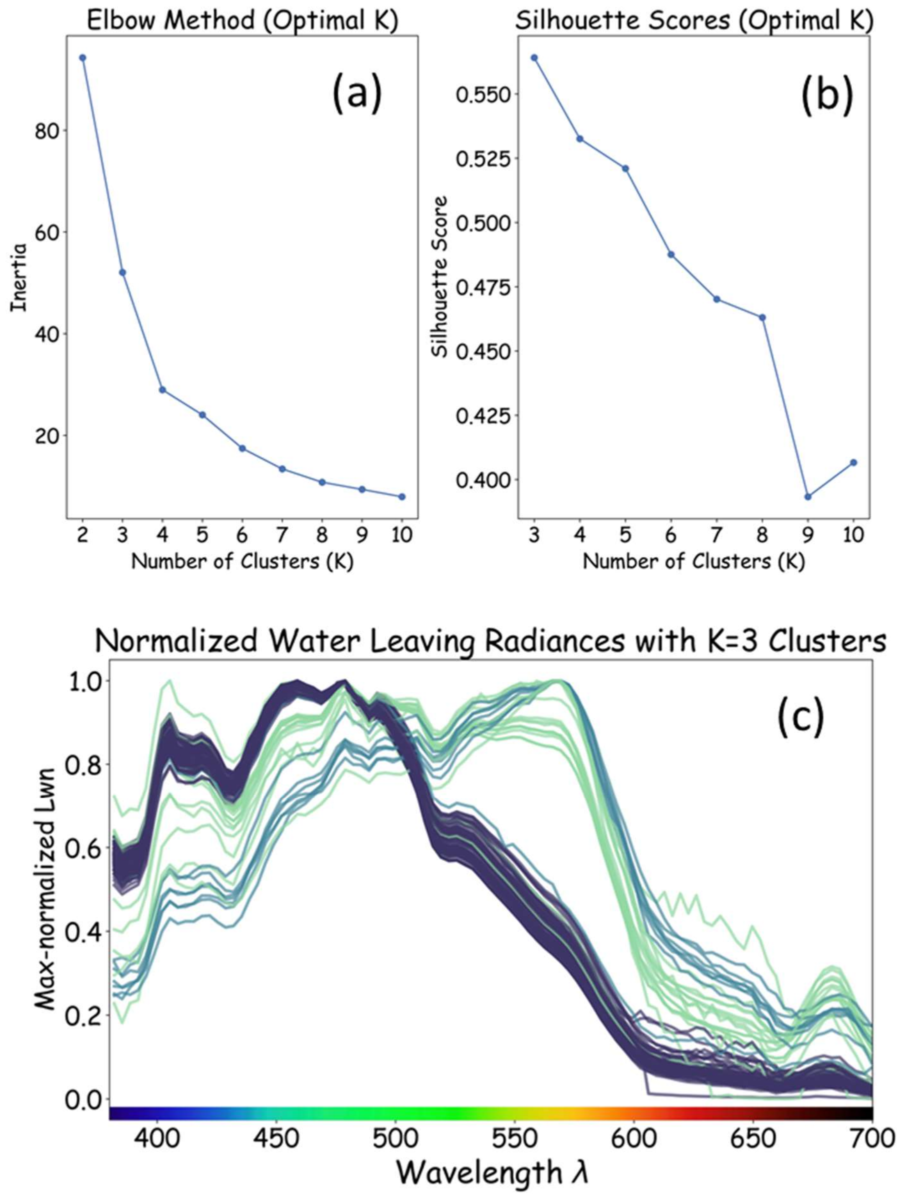


Figure 28. Elbow plot and Silhouette score for all normalized water leaving radiances (max-normalized so all individual spectra are scaled between 0 and 1) for OSU's in-water profilers. Clustered, normalized spectra are seen below with unique colors to represent each cluster. More "pure" oceanic water (dark blue) transitions into a more phytoplankton-detritus-dominated regime (light green) as we get closer to the coast.

Figure 27 shows the normalized $L_w$ radiance observations collected during the cruise. If you look closely, it appears that many of the spectra fall into similar and discrete patterns. This variability is due to the inherent optical properties of the water bodies we encountered off the Oregon coast. While off the Oregon shelf, this effect was mostly due to changes in the concentration and community structure of phytoplankton, although sediments, detritus, and colored dissolved organic matter played an exponentially more important role as we approached the nearshore environment and Columbia River plume. We normalized all spectra by their means to scale values between 0 and 1 before applying *k*-means clustering algorithms to the data. The first was an Elbow method, used to determine the optimal number of clusters for our dataset. When the plot begins to slope towards the right (forming an elbow) it is determined that adding additional clusters does not significantly improve the model (in this case at k=4 clusters) (Figure 28). We followed up on this measure by use of a Silhouette Score, which varies from 1 to −1 with values above 0 representing spectra that more closely match the values of their assigned cluster and less closely match the values of other clusters (values below 0 signal a misclassification).

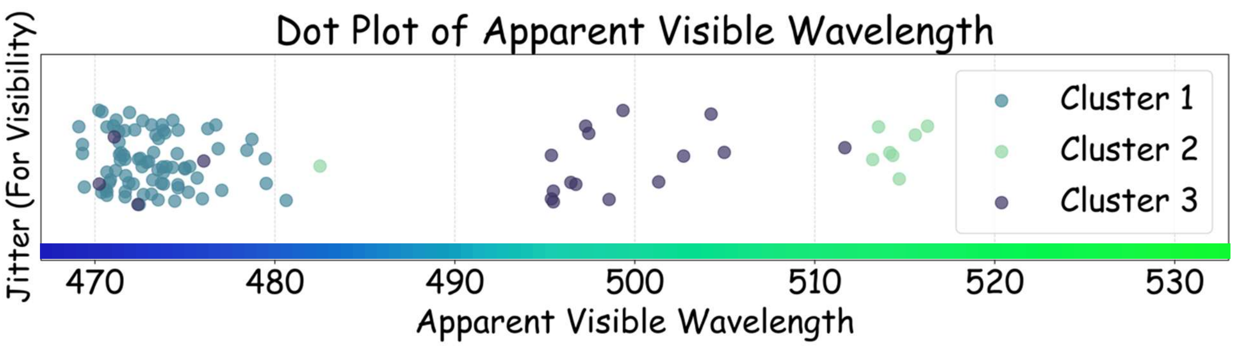


Figure 29. Apparent visible wavelengths of spectra colored by their cluster group. The apparent visible wavelength is a relatively good metric for determining water type as this highly reductive method (going from hundreds of points in a hyperspectral dataset down to one representative wavelength) aligns with the results of the clustering algorithm quite well, with a few exceptions.

Lastly, to aid in the visualization of the reflectance spectra we took an additional dimensionality reduction approach, deriving the Apparent Visible Wavelengths (AVW) for each spectrum via a weighted harmonic mean [*Vandermeulen et al.*, 2020]. The AVW is derived using the following equation:

$$AVW = \frac{\sum_{i=1}^{n} R_{rs}(\lambda_i)}{\sum_{i=1}^{n} \frac{R_{rs}(\lambda_i)}{\lambda_i}} = \left[ \frac{\sum_{i=1}^{n} \lambda_i^{-1} R_{rs}(\lambda_i)}{\sum_{i=1}^{n} R_{rs}(\lambda_i)} \right]^{-1} . \tag{3}$$

The AVW is sensitive to the shape of the spectrum and insensitive to its overall magnitude. Vandermeulen et al. found that in many cases the AVW calculated from multiple imagers and datasets consistently classified the water type based on this one number. Thus, although simple, the AVW is useful for inspecting large datasets, such as the hyperspectral data collected on this cruise. An example of the AVW applied to the normalized water-leaving radiance dataset for the OSU HyperPro is shown below in Figure 29.

### *3.6.2. Inherent optical properties*

Measurements of absorption, scatter, and attenuation (Figure 30) were made with an AC-S, while backscatter was measured using a WET Labs BB3. Instruments were configured in a continuous flow-through in-line system (Figure 31). Water was delivered through the ship's flow-through system into Tygon® tubing which was wrapped in electrical tape to eliminate outside light entering the system. To estimate the contribution of colored dissolved organic matter to the optical properties of the samples, the system was equipped with a filter switch to measure 0.2 μm fractions. Before deployment the inline system was taken apart, 98% isopropyl alcohol was dabbed on AC-S optical windows with lens paper to remove any biofouling, and soap was used for the epoxy windows of the BB3. All instruments were rinsed 3 times with Milli-Q water. Both AC-S tubes were removed and cleaned with lens paper dabbed with isopropyl alcohol using a dowel, they were then rinsed again with Milli-Q. After cleaning, both tubes were gently filled with degassed Milli-Q water being sure to not allow any bubbles to form within the tubes. The data was then logged with the software *Inlinino*, the AC-S was shaken with water inside and caps on, if the spectral shapes remained constant, there were deemed to be no bubbles present. If this was the case a blank baseline water calibration was logged. The AC-S was then disassembled and the cleaning processes were repeated until two baseline calibrations agreed at the 0.005 $m^{-1}$ level. The same process for acquiring baseline calibrations was applied to the BB3, ensuring that the light traps were clean for future measurements.

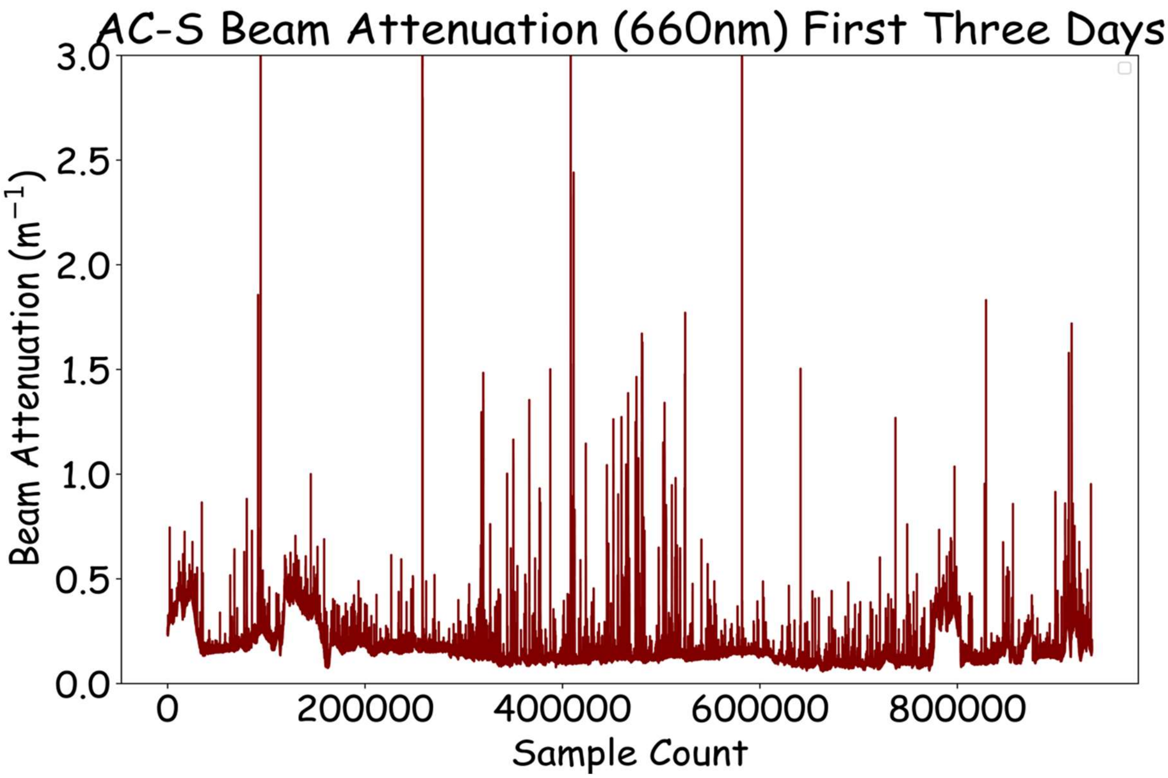


Figure 30. Beam attenuation of red light from the AC-S for the first three days of the cruise for total (unfiltered) seawater. Spikiness is to be expected in these bio-optical data sets when large particles occult the laser.

Figure 31. (Left) An inline system with the AC-S, filters, and tubing, including an aluminum jacket to keep the AC-S at a similar temperature to the water it was measuring, limiting any condensation on the inside of the optical windows. (Right) Computer setup with the logging software used and the light trap for the BB3 in the bottom right corner.

### 3.7. MIAMI – Kenneth J. Voss and E. Riley Blocker

The MIAMI team measured the distribution of polarized radiance for both the sky and water with a spectral polarized radiance distribution camera system, or PixPol [*Blocker and Voss*, 2024]. This instrument derives the first three diffuse Stokes parameters ($I$, $Q$, and $U$) at an angular resolution of 1° within a field of view that encompasses all azimuthal angles up to 43° from the nadir for the in-water upwelling light and 65° for the in-air downwelling light.

During the cruise, data were collected at 20 different locations. At each location, PixPol made measurements for 5–10 minutes, which was enough time to acquire around 30 to 50 images from each camera. However, some images are not suitable for analysis due to various reasons:

- Heavy cloud cover, which when covering the sun, increases the relative contribution from the diffuse light field versus the direct solar beam. Consequently, the light scattered toward PixPol is less likely to come from a well-defined scattering angle. PixPol's downwelling measuring camera allows for easy identification when clouds cover the sun and these instances can be removed. A preprint of an article interpreting the in-water upwelling polarized light field measurements made on this cruise during heavy cloud cover is presented in *Blocker et al.* [2025].
- Heavy seas, which result in large variations in the tilt or roll of PixPol. If PixPol acquires an image when its central optical axis is not aligned with the nadir or zenith direction, georeferencing locations on the image becomes difficult. Also, issues with the distortions due to a different perspective become more prevalent. Images acquired when there was tilt or roll beyond 2.5° from the nadir or zenith direction were removed by comparing the sun's location in the downwelling image with the position predicted by solar ephemeris software for that location and time.
- Breaking waves and bubbles from the ship's propeller generated large amounts of scattered light into the field of view of PixPol. Fortunately, these instances are easily identified by the light signal over-saturating the image.

After removing these occurrences, images from 4 stations (Stations: 11, 16, 17, 18) are suitable for analysis. Given the conditions throughout the entire cruise, the number of stations with usable data is impressive, and I thank the Chief Scientist for his expertise in finding as many places with preferred sky conditions as he did.

An example data set from Station 18 is shown below. At the time of image capture, the solar zenith angle was 56˚. The distribution of $I$, $Q/I$, $U/I$, $DoLP$, and $AoLP$ are shown for the downwelling skylight (Figure 32–Figure 36) and upwelling in-water light (Figure 37–Figure 41). These measurements are compared to the predictions of a single scattering Rayleigh model, which for the upwelling in-water light accounts for the contribution of linearly polarized light from a flat air-water interface. In the images, the origin is indicated with a white and black bull's eye. The solar location is marked with a yellow star with a black outline in the downwelling images. In the in-water upwelling images, the refracted anti-solar location is marked with a black star with a yellow outline. All images are aligned azimuthally so that the sun (anti-solar) location is shown on the right (left) side of the horizontal line passing through the zenith (nadir) direction. Emanating from the solar or anti-solar location are hashed gray lines. The concentric circles are increments of 10° scattering angle measured between the incoming light from the sun and the location it appears on the image. The radial lines are in 30° azimuthal increments. The FOV of the images from the single-scattering theory extends to 90º and the limited FOV of PixPol is represented with the hashed black and white circle.

### 3.7.1. $L_d$ in-air

Images in this section are presented from the $L_d$ in-air camera and compared with a single scattering Rayleigh model.

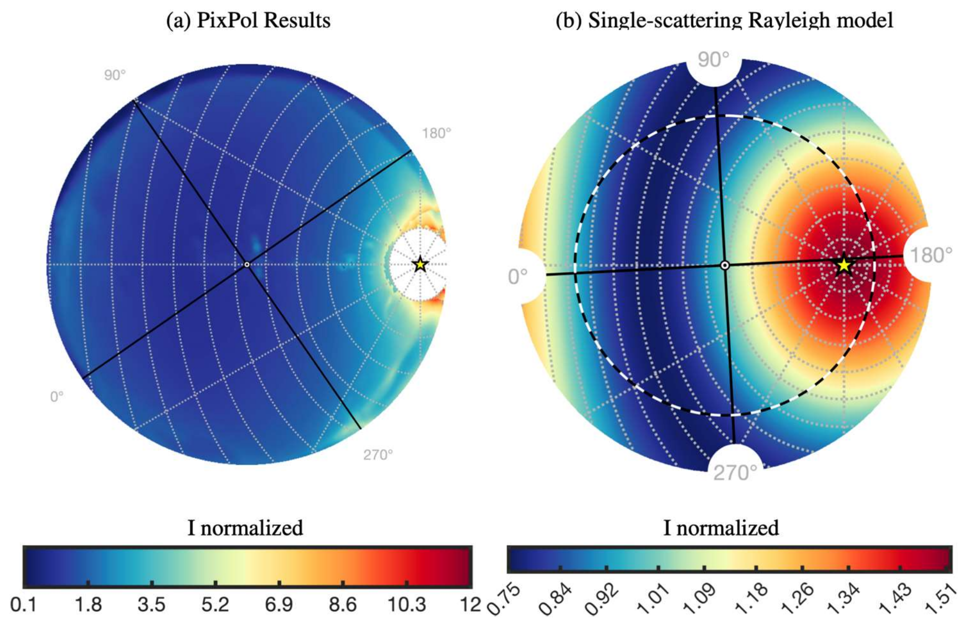


Figure 32. Downwelling $I_{sky}$ ($\lambda$ = 500nm). Values are normalized to the mean value within 2º of the zenith direction. Application of this image is locating the solar position and monitoring cloud conditions.

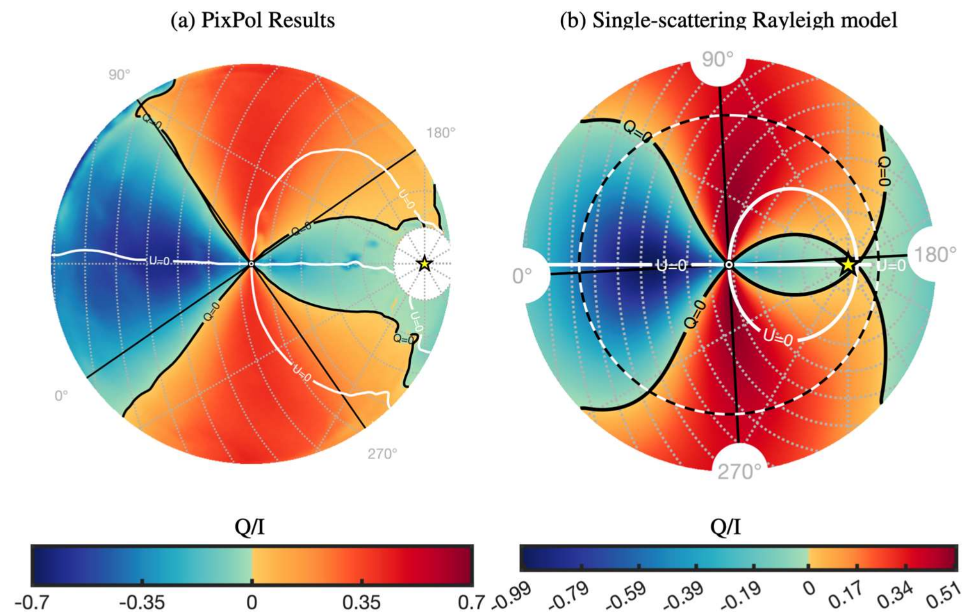


Figure 33. Downelling $Q_{\mathrm{sky}} / I_{\mathrm{sky}}$ ($\lambda$ = 500 nm). In the measured image, the Q=0 line on the solar half does not close the interior of the solar direction and indicates a contribution of light linearly polarized perpendicular to the principal plane.

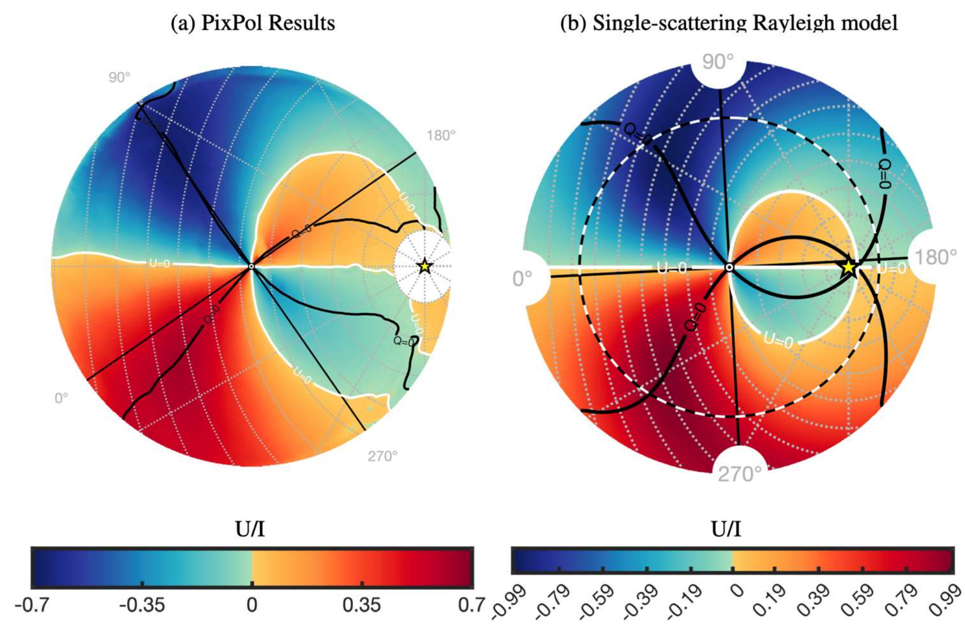


Figure 34. $U_{\mathrm{sky}}$. $/I_{\mathrm{sky}}$ ($\lambda$ = 500 nm).

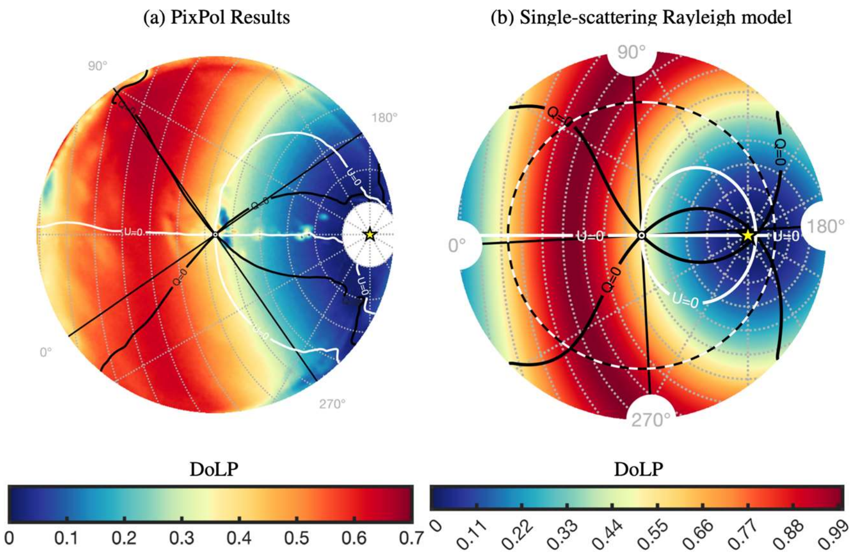


Figure 35. Downwelling $DoLP_{\text{sky}}$ ($\lambda$ = 500 nm). The maximum DoLP occurs near a 90˚ scattering angle as predicted by the single-scattering Rayleigh model. However, unlike the model, the measured the Q=U=0 location does not occur along the principal plane.

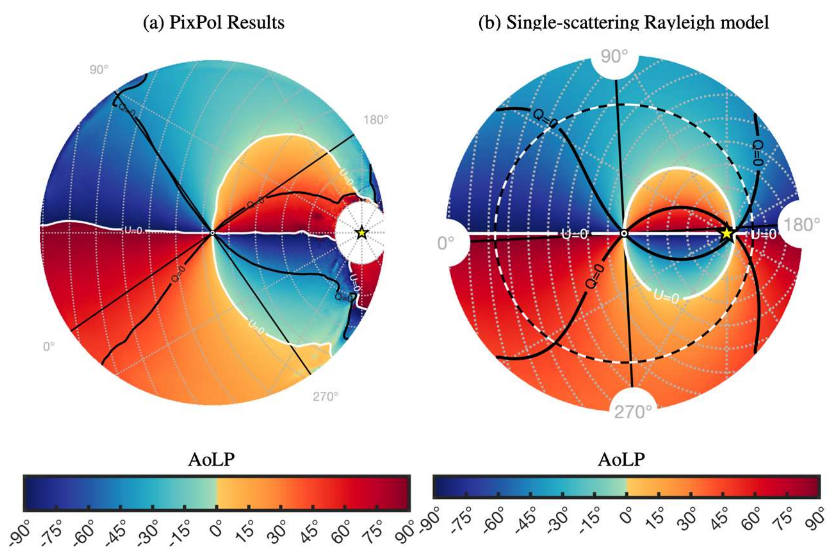


Figure 36. Downwelling $AoLP_{\text{sky}}$ ($\lambda$ = 500 nm).

### *3.7.2. $L_u$ in-water*

Images in this section are presented from the upwelling in-water camera and compared with a single scattering Rayleigh model that accounts for the propagation of unpolarized light through a flat air-water interface. PixPol also measures in the 444 nm and the 500 nm spectral regions, but only measurements from the 670 nm camera are shown here.

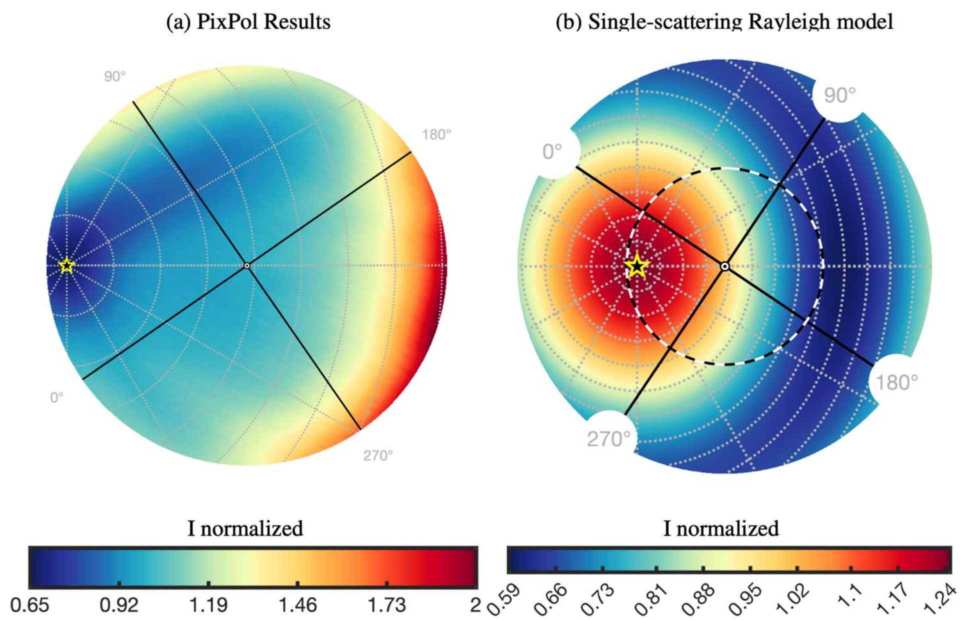


Figure 37. In-water upwelling $I_{water}(\lambda = 670$ nm). In the measured image, low radiance values are measured in the vicinity of the refracted anti-solar location where the instrument self-shading occurs. Values are normalized to the mean value within 2° of the nadir direction.

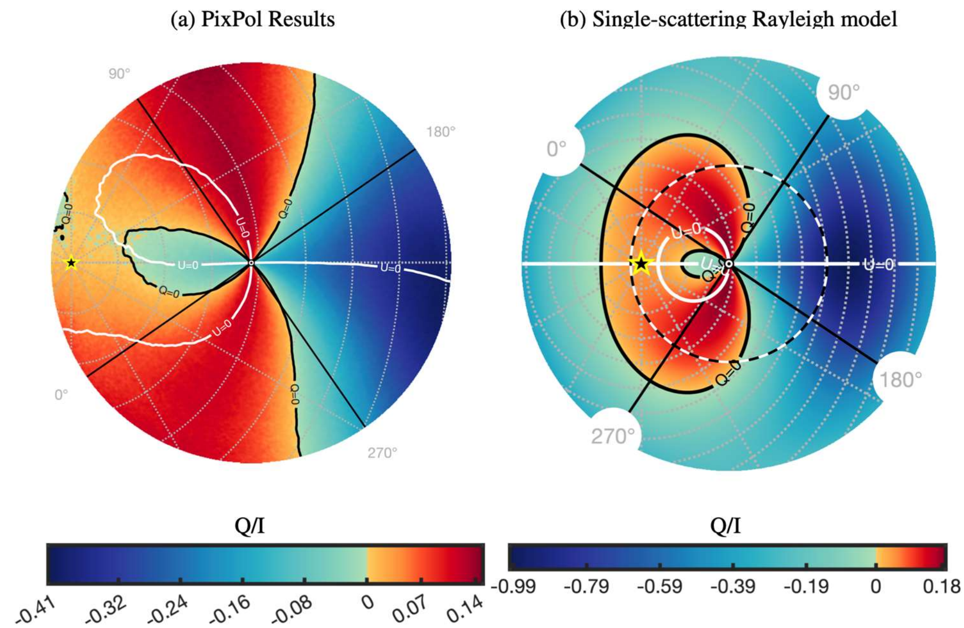


Figure 38. In-water upwelling $Q_{\text{water}} / I_{\text{water}}$ ($\lambda$ = 670 nm).

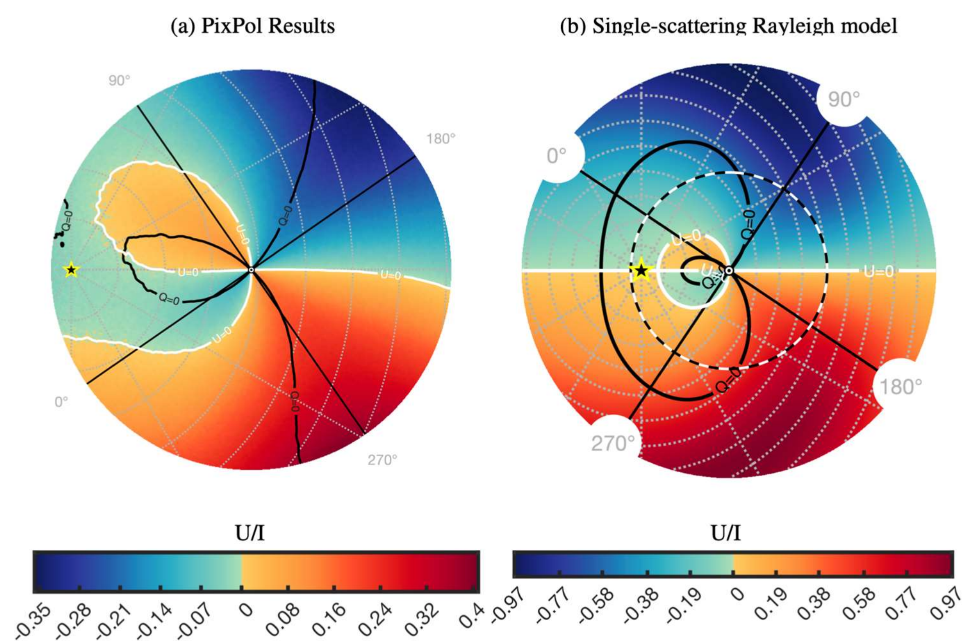


Figure 39. In-water upwelling $U_{\text{water}} / I_{\text{water}}$ ($\lambda$ = 670 nm).

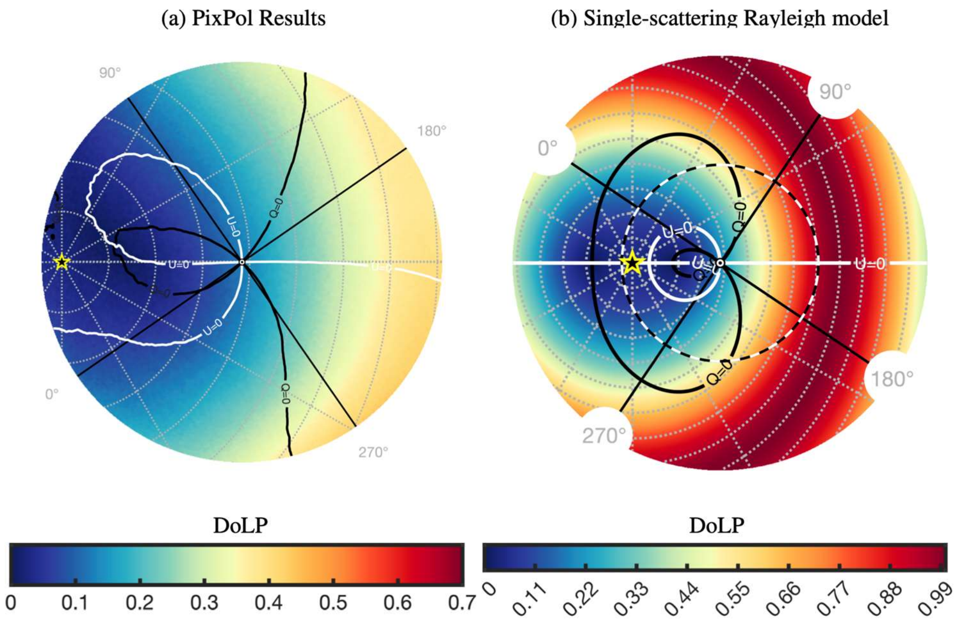


Figure 40. In-water upwelling $DoLP_{\mathrm{water}}$ ($\lambda$ = 670 nm). The measured Q=U=0 location occurs interior of the refracted anti-solar point near the principal plane.

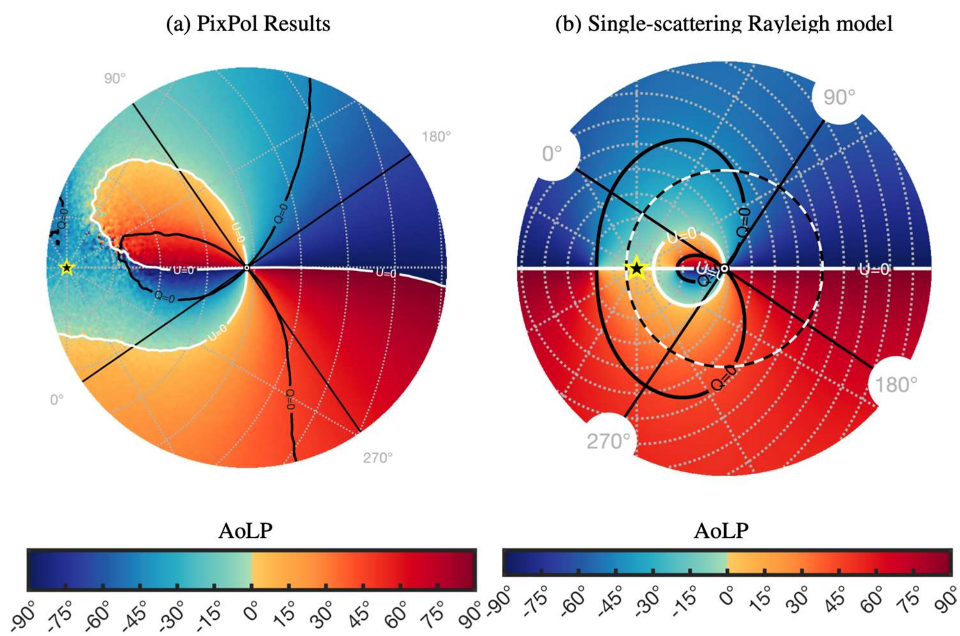


Figure 41. In-water upwelling $AoLP_{\mathrm{water}}$ ($\lambda$ =670 nm).

# 4. Data Comparison and Validation

The $R_{rs}$ measurements from two profiling radiometers and two above-water radiometers are shown in Figure 42. As a qualitative comparison, the $R_{rs}$ spectra from profilers are in good agreement. 80% of them suggest that the water types belong to Class 4–6. For the remaining stations, the water types can be described as Class 10–12. The example above-water $R_{rs}$ measurements are more variable due to surface contamination than the in-water profiling measurements. Specifically, the SEI spectral $R_{rs}$ is the least variable with better comparisons to both HyperPro profiling radiometers.

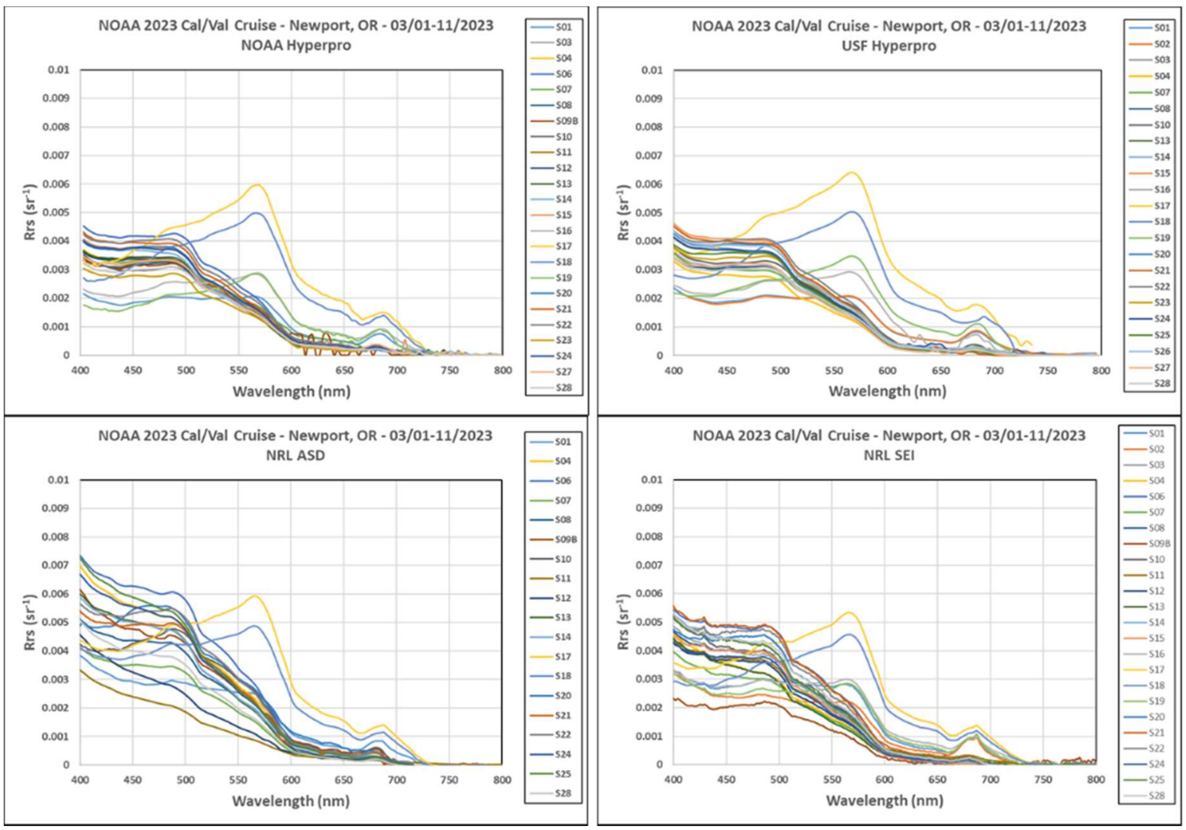


Figure 42. $R_{rs}$ spectra collected by the NOAA (top left) and USF (top right) profiling HyperPro’s and NRL’s above-water ASD (bottom left) and SEI (bottom right) radiometers. Legends are given for the station numbers.

Figure 43A shows preliminary spectral $R_{rs}(\lambda)$ comparisons between NOAA's HyperPro data and USF's HyperPro results at five wavelengths for all 24 stations. The USF HyperPro data are slightly higher at all wavelengths than NOAA's HyperPro data. This difference varies between 1–5% at blue and green bands, and larger at red bands mostly because Rrs values are very small at longer wavelengths at these stations.

Figure 43B shows the same preliminary spectral $R_{rs}(\lambda)$ comparisons for the SEI data and the combined HyperPro data. The NOAA HyperPro was used for 21 stations and the USF was substituted for the other 3 stations due to issues with the NOAA HyperPro. The SEI $R_{rs}(\lambda)$ measurements are slightly higher than the HyperPro measurements. Considering the difficulty with above-water radiometry, the degree of agreement between these two data sets is indeed high.

Figure 43C shows the same preliminary spectral $R_{rs}(\lambda)$ comparisons for the ASD results and the combined HyperPro data. The ASD $R_{rs}(\lambda)$ measurements are higher than the Hyperpro measurements to an elevated degree. The differences are found to vary from 23% at green wavelengths to 45% at blue wavelengths.

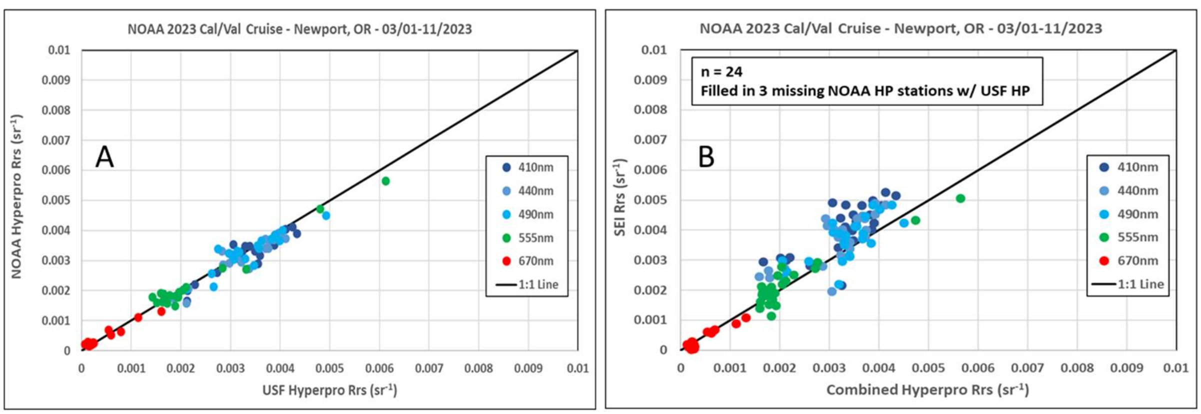


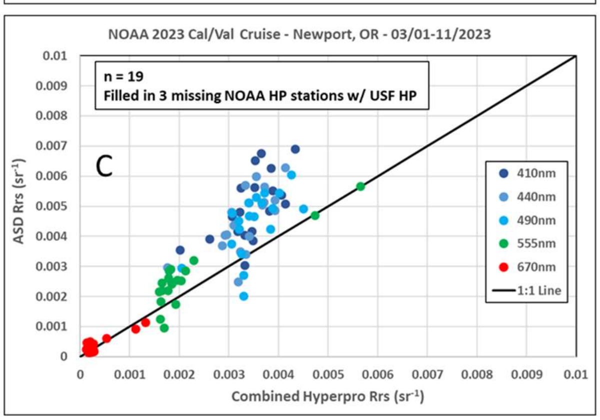


| *SLOPE* | *Rrs410* | *Rrs440* | *Rrs490* | *Rrs555* | *Rrs670* |
|---|---|---|---|---|---|
| USF, NOAA HP | 0.94 | 0.95 | 0.97 | 0.96 | 0.92 |
| NRL ASD, HP | 1.44 | 1.37 | 1.27 | 1.14 | 0.97 |
| NRL SEI, HP | 1.21 | 1.15 | 1.09 | 0.99 | 0.86 |
| *RSQ* | *Rrs410* | *Rrs440* | *Rrs490* | *Rrs555* | *Rrs670* |
| USF, NOAA HP | 0.84 | 0.82 | 0.76 | 0.96 | 0.92 |
| NRL ASD, HP | 0.38 | 0.46 | 0.38 | 0.72 | 0.63 |
| NRL SEI, HP | 0.47 | 0.55 | 0.49 | 0.84 | 0.91 |
| *RATIO* | *Rrs410* | *Rrs440* | *Rrs490* | *Rrs555* | *Rrs670* |
| USF, NOAA HP | 1.05 | 1.04 | 1.02 | 1.01 | 0.84 |
| NRL ASD, HP | 1.45 | 1.37 | 1.28 | 1.23 | 1.25 |
| NRL SEI, HP | 1.25 | 1.19 | 1.11 | 1.04 | 0.84 |

Figure 43. Scatterplots of in situ determination of $R_{rs}$ during the Cal/Val cruise. The table (bottom right) gives the statistics (slope, $r^2$, and ratio) for each comparison. "HP" and "RSQ" in the table refer to HyperPro and $r^2$, respectively.

In Figure 44, the spectral matchups are presented at each station among the HyperPro data (black line), the SEI measurements (gray line), NRL-processed satellite data (SNPP denoted in green circles, NOAA-20 data in blue circles, and NOAA-21 data in purple circles), and NOAA-processed satellite data (SNPP in yellow circles and NOAA-20 in red circles). Note if one of the satellite matchups is missing, they are either cloudy or glint-contaminated. Matchups between NRL and NOAA VIIRS sensors and in- and above-water $R_{rs}(\lambda)$ show good agreement even though the sea state, weather, and light conditions were unfavorable most of the time. Out of 27 stations, there were 17 stations with at least one VIIRS matchup for NRL APS processing (due to more relaxed cloud screening than NOAA MSL12 processing).

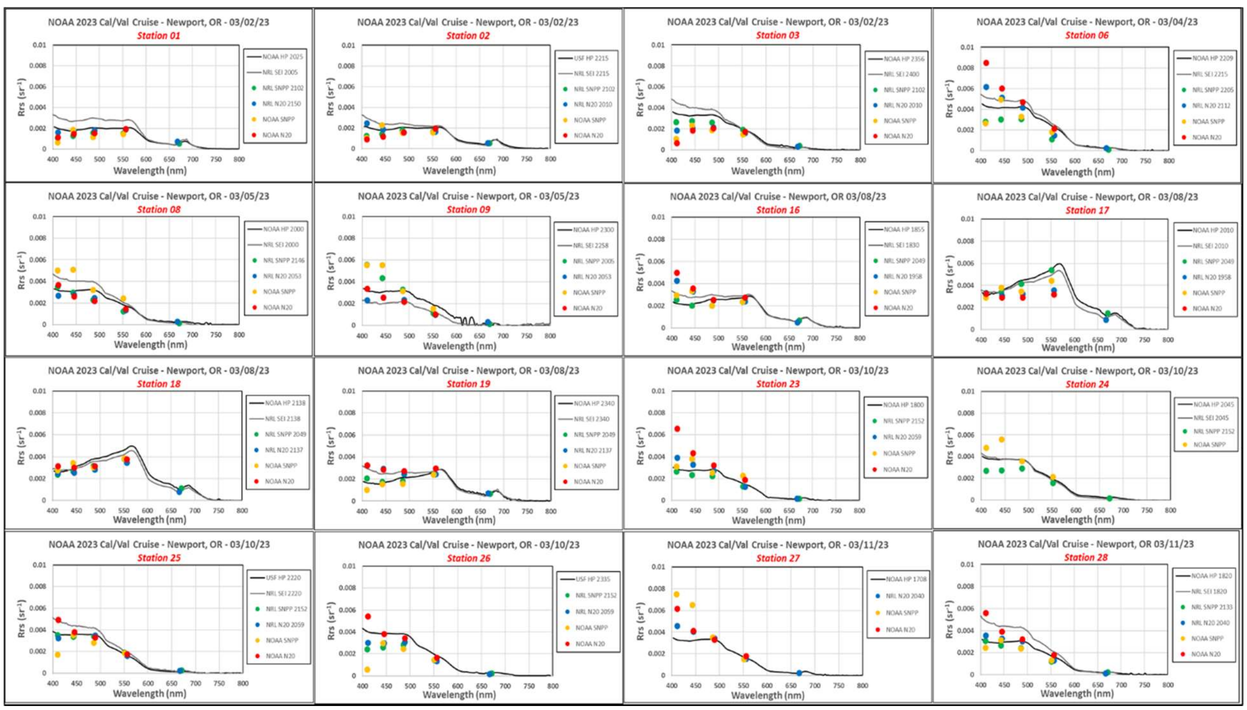


Figure 44. Comparison of the $R_{rs}$ spectra measured in situ and satellites during the Cal/Val cruise.

## 5. Summary

The eighth dedicated VIIRS Cal/Val cruise was successfully conducted in the northern California Current in early 2023. The main objective was to measure the remote sensing reflectance and normalized water-leaving radiances to evaluate and improve the VIIRS ocean color products from the SNPP, NOAA-20, and NOAA-21 satellites. In addition, in situ data from the dedicated Cal/Val cruise can also be used for evaluation and validation of ocean color product data from other satellite sensors, e.g., OLCI on Sentinel-3A/3B and SGLI on GCOM-C. A combination of in-water radiometric profilers, above-water radiometers, flow-through IOP sensors, and discrete water sampling were deployed and implemented. The in situ observations also included the phytoplankton cell identification and sizing as well as the polarized upwelling radiance distribution. Despite the rough seas and logistic challenges, the field team successfully collected a wide range of data from 28 stations. The obtained data will support the validation and calibration of the NOAA satellite-based ocean color observations and also help better understand the bio-optical variability and complexity in these ocean environments. The fully processed in situ data can be accessible upon approval.

## Acknowledgments

The VIIRS ocean color Cal/Val science team is grateful for the support of NOAA OMAO. Individual team leads were funded either by the JPSS ocean color projects or external funding. We thank the crew of the NOAA Ship *Bell M. Shimada* for their effort in making data collection possible. The scientific results and conclusions, as well as any views or opinions expressed herein, are those of the author(s) and do not necessarily reflect those of NOAA or the Department of Commerce.

## References

Blocker, E. R., J. Hedley, and M. Twardowski (2025), Neutral lines and model-measurement closure in oceanic polarized light fields, *Optica Open. Preprint*, 10.1364/opticaopen.28533689.v1.

Blocker, E. R., and K. J. Voss (2024), PixPol: an in-water multispectral polarized upwelling radiance distribution camera system, *J. Atmos. Ocean. Technol.*, *41*(11), 1081-1092, https://doi.org/10.1175/JTECH-D-24-0022.1.

Carder, K. L., and R. G. Steward (1985), A remote-sensing reflectance model of a red tide dinoflagellate off West Florida, *Limnol. Oceanogr.*, *30*, 286-298.

Chekalyuk, A. M., and M. Hafez (2008), Advanced laser fluorometry of natural aquatic environments, *Limnol. Oceanogr.: Methods*, *6*(11), 591-609, https://doi.org/10.4319/lom.2008.6.591.

Chekalyuk, A. M., M. R. Landry, R. Goericke, A. G. Taylor, and M. A. Hafez (2012), Laser fluorescence analysis of phytoplankton across a frontal zone in the California Current ecosystem, *Journal of Plankton Research*, *34*(9), 761-777, 10.1093/plankt/fbs034.

Cox, C., and W. Munk (1954), Measurement of the roughness of the sea surface from photographs of the sun's glitter, *J. Opt. Soc. Am.*, *44*(11), 838-850.

Goes, J. I., H. d. R. Gomes, E. M. Haugen, K. T. McKee, E. J. D'Sa, A. M. Chekalyuk, D. K. Stoecker, P. J. Stabeno, S.-I. Saitoh, and R. N. Sambrotto (2014), Fluorescence, pigment and microscopic characterization of Bering Sea phytoplankton community structure and photosynthetic competency in the presence of a Cold Pool during summer, *Deep Sea Research Part II: Topical Studies in Oceanography*, *109*, 84-99, https://doi.org/10.1016/j.dsr2.2013.12.004.

Gorbunov, M. Y., and P. G. Falkowski (2004), Fluorescence induction and relaxation (FIRe) technique and instrumentation for monitoring photosynthetic processes and primary production in aquatic ecosystems, paper presented at Photosynthesis: Fundamental Aspects to Global Perspectives"-Proc. 13th International Congress of Photosynthesis, Montreal, Aug.

Gordon, H. R., and M. Wang (1994), Retrieval of water-leaving radiance and aerosol optical thickness over the oceans with SeaWiFS: a preliminary algorithm, *Appl. Opt.*, *33*(3), 443-452.

Hickey, B. M., and N. S. Banas (2008), Why is the northern end of the California Current System so productive?, *Oceanography*, *21*(4), 90-107.

Holm-Hansen, O., and B. Riemann (1978), Chlorophyll a determination: improvements in methodology, *Oikos*, *30*, 438-447.

IOCCG (2010), Atmospheric correction for remotely-sensed ocean color products. M. Wang (Ed.), Reports of the International Ocean-Colour Coordinating Group *No. 10*, 78 pp. International Ocean Color Coordinating Group, Dartmouth, Nova Scotia, Canada, https://doi.org/10.25607/OBP-101.

Jenkins, C., et al. (2016), High-resolution shipboard measurements of phytoplankton: a way forward for enhancing the utility of satellite SST and chlorophyll for mapping microscale features and frontal zones in coastal waters, *Proc. SPIE*, *9878*, 10.1117/12.2225875.

Kishino, M., M. Takahashi, N. Okami, and S. Ichimura (1985), Estimation of the spectral absorption coefficients of phytoplankton in the sea, *Bulletin of Marine Science*, *37*(2), 634-642.

Malinowski, M., A. Gilerson, E. Herrera-Estrella, and J. Agagliate (2023), Polarimetric imaging of the ocean surface for the study of ocean surface roughness and wave slopes statistics, *Proc. SPIE*, *12543*, https://doi.org/10.1117/12.2665834.

Malinowski, M., A. Gilerson, E. Herrera-Estrella, R. Foster, J. Agagliate, and M. Ondrusek (2024a), Surface roughness and wave slope statistics from the multi-spectral polarimetric imaging of the ocean surface, *Opt. Express*, *32*(13), 22110-22131, 10.1364/OE.521650.

Malinowski, M., A. Gilerson, E. Herrera-Estrella, R. Foster, A. Ibrahim, J. Agagliate, and M. Ondrusek (2024b), Uncertainties in radiometric measurements of the ocean surface from above water and helicopter hyperspectral and polarimetric observations, *Appl. Opt.*, *63*(23), 6097-6111, 10.1364/AO.527229.

Mobley, C. D. (1999), Estimation of the remote-sensing reflectance from above-surface measurements, *Appl. Opt.*, *38*(36), 7442-7455.

Mobley, C. D. (2015), Polarized reflectance and transmittance properties of windblown sea surfaces, *Appl. Opt.*, *54*(15), 4828-4849, 10.1364/AO.54.004828.

Mueller, J. L., G. S. Fargion, and C. R. McClain (2003a), Ocean Optics Protocols For Satellite Ocean Color Sensor Validation, Revision 4, NASA, Goddard Space Flight Center, Greenbelt, MD.

Mueller, J. L., G. S. Fargion, and C. R. McClain (2003b), Radiometric measurements and data analysis protocols. Ocean optics protocols for satellite ocean color sensor validation, Revision 4, *No. NASA/TM-2003-21621/Rev-Vol III*, 84 pp. NASA Goddard Space Flight Center, Greenbelt, MD.

Nalli, N. R., et al. (2022), Ship-based cal/val campaigns, in *Field measurements for passive environmental remote sensing: Instrumentation, intensive campaigns, and satellite applications*, edited by N. R. Nalli, pp. 195-217, Elsevier, doi:https://doi.org/10.1016/B978-0-12-823953-7.00008-3.

Ondrusek, M., et al. (2015), Report for dedicated JPSS VIIRS Ocean Color Calibration/Validation Cruise. V. P. Lance (Ed.), NOAA Tech. Rep. NESDIS *No. 146*, 60 pp. NOAA National Environmental Satellite, Data, and Information Service, Washington, D.C., https://doi.org/10.7289/V52B8W0Z.

Ondrusek, M., et al. (2016), Report for dedicated JPSS VIIRS Ocean Color December 2015 Calibration/Validation Cruise. V. P. Lance (Ed.), NOAA technical report NESDIS 148 *No. 148*, 66 pp. United States, National Environmental Satellite, Data, and Information Service, Silver Spring, Maryland, 10.7289/V5/TR-NESDIS-148.

Ondrusek, M., et al. (2017), Report for dedicated JPSS VIIRS Ocean Color Calibration/Validation Cruise, October 2016. V. P. Lance (Ed.), NOAA Tech. Rep. NESDIS *No. 151*, 65 pp. United States. National Environmental Satellite, Data, and Information Service, Washington, D.C., https://doi/org/10.7289/V5/TR-NESDIS-151.

Ondrusek, M., et al. (2019), Report for Dedicated JPSS VIIRS Ocean Color Calibration/Validation Cruise May 2018. V. P. Lance (Ed.), NOAA Tech. Rep. NESDIS *No. 152*, 91 pp. United States. National Environmental Satellite, Data, and Information Service, Washington, D.C., https://doi.org/10.25923/scyb-qf42.

Ondrusek, M., et al. (2021), Report for dedicated JPSS VIIRS ocean color calibration/validation cruise September 2019. V. P. Lance (Ed.), NOAA Tech. Rep. NESDIS *No. 154*, 60 pp. National Environmental Satellite, Data, and Information Service (NESDIS), Washington D. C., https://doi.org/10.25923/p9de-yw97.

Ondrusek, M., et al. (2022), Report for dedicated JPSS VIIRS ocean color calibration/validation cruise: Gulf of Mexico in April 2021. J. Wei (Ed.), NOAA Tech. Rep. NESDIS *No. 157*, 51 pp. NOAA National Environmental Satellite, Data Information, Service, Washington D. C., United States, https://doi.org/10.25923/x2q6-9418.

Ondrusek, M., et al. (2024), Report for dedicated JPSS VIIRS ocean color calibration/validation cruise : Hawaii in March 2022. J. Wei (Ed.), NOAA Tech. Rep. NESDIS *No. 160*, 68 pp. NOAA/NESDIS Center for Satellite Applications and Research, Washington, D. C., https://doi.org/10.25923/g8wq-0g19.

Perez, R. C., G. R. Foltz, R. Lumpkin, J. Wei, K. J. Voss, M. Ondrusek, M. Wang, and M. A. Bourassa (2022), Oceanographic buoys: Providing ocean data to assess the accuracy of variables derived from satellite measurements, in *Field Measurements for Passive Environmental Remote Sensing*, edited by N. R. Nalli, pp. 79-100, Elsevier, doi:10.1016/B978-0-12-823953-7.00022-8.

Ryther, J. H. (1969), Photosynthesis and fish production in the sea, *Science*, *166*(3901), 72-76, doi:10.1126/science.166.3901.72.

Shi, W., and M. Wang (2019), A blended inherent optical property algorithm for global satellite ocean color observations, *Limnol. Oceanogr.: Methods*, *17*(7), 377-394, https://doi.org/10.1002/lom3.10320.

Son, S., and M. Wang (2015), Diffuse attenuation coefficient of the photosynthetically available radiation Kd(PAR) for global open ocean and coastal waters, *Remote Sens. Environ.*, *159*, 250-258, https://doi.org/10.1016/j.rse.2014.12.011.

Vandermeulen, R. A., A. Mannino, S. E. Craig, and P. J. Werdell (2020), 150 shades of green: Using the full spectrum of remote sensing reflectance to elucidate color shifts in the ocean, *Remote Sens. Environ.*, *247*, 111900, 10.1016/j.rse.2020.111900.

Wang, M. (2007), Remote sensing of the ocean contributions from ultraviolet to near-infrared using the shortwave infrared bands: simulations, *Appl. Opt.*, *46*(9), 1535-1547, https://doi.org/10.1364/AO.46.001535.

Wang, M., W. Shi, L. Jiang, and K. Voss (2016), NIR- and SWIR-based on-orbit vicarious calibrations for satellite ocean color sensors, *Opt. Express*, *24*(18), 20437-20453, https://doi.org/10.1364/OE.24.020437.

Wang, M., and S. Son (2016), VIIRS-derived chlorophyll-a using the ocean color index method, *Remote Sens. Environ.*, *182*, 141-149, https://doi.org/10.1016/j.rse.2016.05.001.

Wei, J., Z. P. Lee, and S. Shang (2016), A system to measure the data quality of spectral remote sensing reflectance of aquatic environments, *J. Geophys. Res.*, *121*(11), 8189–8207, https://doi.org/10.1002/2016JC012126.

Wei, J., M. Wang, L. Jiang, X. Yu, K. Mikelsons, and F. Shen (2021), Global estimation of suspended particulate matter from satellite ocean color imagery, *J. Geophys. Res.*, *126*(8), https://doi.org/10.1029/2021JC017303.

Wei, J., M. Wang, K. Mikelsons, L. Jiang, S. Kratzer, Z. P. Lee, T. Moore, H. M. Sosik, and D. Van der Zande (2022), Global satellite water classification data products over oceanic, coastal, and inland waters, *Remote Sens. Environ.*, *282*, https://doi.org/10.1016/j.rse.2022.113233.

Wei, J., et al. (2023), Satellite ocean color validation, in *Field measurements for passive environmental remote sensing: instrumentation, intensive campaigns, and satellite applications*, edited by N. Nalli, pp. 351-374, Elsevier, Cambridge, MA, United States, doi:https://doi.org/10.1016/B978-0-12-823953-7.00006-X.

Welschmeyer, N. A. (1994), Fluorometric analysis of chlorophyll-*a* in the presence of chlorophyll-*b* and pheopigments, *Limnol. Oceanogr.*, *39*(8), 1985-1992.

Werdell, P. J., S. W. Bailey, B. A. Franz, A. Morel, and C. R. McClain (2007), On-orbit vicarious calibration of ocean color sensors using an ocean surface reflectance model, *Appl. Opt.*, *46*, 5649-5666.

Zappa, C. J., M. L. Banner, H. Schultz, A. Corrada-Emmanuel, L. B. Wolff, and J. Yalcin (2008), Retrieval of short ocean wave slope using polarimetric imaging, *Measurement Science and Technology*, *19*, 13pp.

Zibordi, G., et al. (2025), System vicarious calibration for climate and global long-term operational ocean color applications, *Bull. Amer. Meteor. Soc.*, *106*(2), E394-E407, https://doi.org/10.1175/BAMS-D-24-0085.1.

Zibordi, G., F. Mélin, J. M. Voss, B. C. Johnson, B. A. Franz, E. J. Kwiatkowska, J.-P. Huot, M. Wang, and D. Antoine (2015), System vicarious calibration for ocean color climate change applications: requirements for in situ data, *Remote Sens. Environ.*, *159*, 361-369.

## Appendices: Symbols, Abbreviations, and Acronyms

Table A1. List of symbols and descriptions

| Symbol | Description | Units |
|---|---|---|
| $a$ | Light absorption coefficient | $m^{-1}$ |
| $a_d$ | Light absorption coefficient by detrital matter | $m^{-1}$ |
| $a_g$ | Light absorption coefficient by CDOM | $m^{-1}$ |
| $a_p$ | Light absorption coefficient by particles | $m^{-1}$ |
| $a_{pg}$ | Light absorption coefficient by CDOM and detritus | $m^{-1}$ |
| $a_{ph}$ | Light absorption coefficient by phytoplankton | $m^{-1}$ |
| $a^{*}_{ph}$ | Chlorophyll-specific phytoplankton absorption coefficient | $m^2\ mg^{-1}$ |
| $b$ | (total) Light scattering coefficient | $m^{-1}$ |
| $b_b$ | Backscattering coefficient of particles | $m^{-1}$ |
| *Chl-a* | Chlorophyll-a concentration | $mg\ m^{-3}$ |
| $E_d$ | Downwelling irradiance | $mW\ cm^{-2}\ \mu m^{-1}$ |
| $E_s$ | Downwelling irradiance just above the water surface | $mW\ cm^{-2}\ \mu m^{-1}$ |
| $K_d$ | Diffuse attenuation coefficient for downwelling irradiance | $m^{-1}$ |
| $L_{surf}$ | Total radiance from the water surface | $mW\ cm^{-2}\ \mu m^{-1}\ sr^{-1}$ |
| $L_{sky}$ | Radiance of sky | $mW\ cm^{-2}\ \mu m^{-1}\ sr^{-1}$ |
| $L_u$ | Upwelling radiance | $mW\ cm^{-2}\ \mu m^{-1}\ sr^{-1}$ |
| $L_u(0^{-},\lambda)$ | Spectral upwelling radiance just below the water surface | $mW\ cm^{-2}\ \mu m^{-1}\ sr^{-1}$ |
| $L_w$ | Water-leaving radiance | $mW\ cm^{-2}\ \mu m^{-1}\ sr^{-1}$ |
| $nL_w$ | Normalized water-leaving radiance | $mW\ cm^{-2}\ \mu m^{-1}\ sr^{-1}$ |
| $R_{rs}$ | Remote sensing reflectance | $sr^{-1}$ |
| $W_s$ | Wind speed | m/s |
| $\lambda$ | Wavelength | nm |
| $\varphi$ | Relative azimuth of the sensor to the sun | deg |
| $\rho$ | Fresnel reflectance factor of seawater | |
| $\theta$ | Zenith Angle | deg |
| $\theta_s$ | Solar-zenith Angle | deg |

Table A2. List of abbreviations and acronyms

| Name | Description |
|---|---|
| AC | Atmospheric correction |
| ADCP | Acoustic Doppler Current Profiler |
| AERONET-OC | Aerosol Robotic Network-Ocean Color |
| AoLP | Angle of Linear Polarization |
| AOP | Apparent optical property |
| AOT | Aerosol optical thickness |
| AVW | Apparent visible wavelength |
| BRDF | Bidirectional reflectance distribution function |
| Cal/Val | Calibration and Validation |
| CCNY | City College of New York |
| CCS | California Current System |
| CDOM | Colored dissolved organic material |
| Chl-a | Chlorophyll-a concentration |
| DoLP | Degree of linear polarization |
| EDR | Environmental Data Record |
| FOV | Field of view |
| FWHM | Full width at half maximum |
| GPS | Global Positioning System |
| HPLC | High Pressure Liquid Chromatography |
| IFOV | Instantaneous field of view |
| HTSRB | Hyperspectral tethered spectral radiometric buoy |
| IOP | Inherent optical property |
| JPSS | Joint Polar Satellite System |
| LDEO | Lamont-Doherty Earth Observatory at Columbia University |
| MSL12 | Multi-Sensor Level-1 to Level-2 |

Table A3. A continuation of Table A2

| Name | Description |
|---|---|
| NESDIS | National Environmental Satellite, Data, and Information Service |
| NIR | Near-infrared |
| NIST | National Institute of Standards and Technology |
| NRL | Naval Research Laboratory |
| NOAA | National Oceanic and Atmospheric Administration |
| OC | Ocean Color |
| OLCI | Ocean and Land Colour Instrument |
| OMAO | Office of Marine and Air Operations |
| OSU | Oregon State University |
| PAR | Photosynthetically available radiation (400–700 nm) |
| PFT | Phytoplankton Functional Type |
| SBA | Skylight-blocking apparatus |
| SGLI | Second Generation Global Imager |
| SNPP | Suomi National Polar-orbiting Partnership |
| SPM | Suspended Particulate Matter |
| SST | Sea surface temperature |
| STAR | Center for Satellite Applications and Research |
| SWIR | Shortwave infrared |
| USF | University of South Florida |
| UV | Ultraviolet |
| VIIRS | Visible Infrared Imaging Radiometer Suite |